

The High A_V Quasar Survey: reddened Quasi Stellar Objects selected from optical/near-infrared photometry - II ¹

J.-K. Krogager^{2,3}, S. Geier⁴, J. P. U. Fynbo², B. Venemans⁵, P. Noterdaeme⁶, M. Vestergaard^{2,7}, C. Ledoux³, P. Møller⁸, F. G. Saturni^{8,9}, O. Smirnova^{4,10}, T. Kangas^{4,11}, J. Telting⁴, T. Pursimo⁴

ABSTRACT

Quasi Stellar Objects (QSOs) whose spectral energy distributions (SEDs) are reddened by dust either in their host galaxies or in intervening absorber galaxies are to a large degree missed by optical colour selection criteria like the one used by the Sloan Digital Sky Survey (SDSS). To overcome this bias against red QSOs, we employ a combined optical and near-infrared colour selection. In this paper, we present a spectroscopic follow-up campaign of a sample of red candidate QSOs which were selected from the SDSS and the UKIRT Infrared Deep Sky Survey (UKIDSS). The spectroscopic data and SDSS/UKIDSS photometry are supplemented by mid-infrared photometry from the Wide-field Infrared Survey Explorer (WISE). In our sample of 159 candidates, 154 (97%) are confirmed to be QSOs. We use a statistical algorithm to identify sightlines with plausible intervening absorption systems and identify 9 such cases assuming dust in the absorber similar to Large Magellanic Cloud sightlines. We find absorption systems towards 30 QSOs, two of which are consistent with the best-fit absorber redshift from the statistical modelling. Furthermore, we observe a broad range in SED properties of the QSOs as probed by the rest-frame $2\ \mu\text{m}$ flux. We find QSOs with a strong excess as well as QSOs with a large deficit at rest-frame $2\ \mu\text{m}$ relative to a QSO template. Potential solutions to these discrepancies are discussed. Overall, our study demonstrates the high efficiency of the optical/near-infrared selection of red QSOs.

²Dark Cosmology Centre, Niels Bohr Institute, University of Copenhagen, Juliane Maries Vej 30, DK-2100 Copenhagen Ø

³European Southern Observatory, Alonso de Córdova 3107, Vitacura, Casilla 19001, Santiago 19, Chile

⁴Nordic Optical Telescope, Apartado 474, 38700 Santa Cruz de La Palma, Spain

⁵Max-Planck Institute for Astronomy, Königstuhl 17, 69117 Heidelberg, Germany

⁶CNRS-UPMC, UMR7095, Institut d'Astrophysique de Paris, 98bis bd Arago, 75014, Paris, France

⁷Steward Observatory and Department of Astronomy, University of Arizona, 933 N Cherry Avenue, Tucson, AZ 85721, USA

⁸European Southern Observatory, Karl-Schwarzschildstrasse 2, D-85748 Garching bei München, Germany

⁹University of Rome "La Sapienza", p.le A. Moro 5, I-00185 Rome, Italy

¹⁰Institute of Astronomy, University of Latvia, Raina bulv. 19, Riga, LV 1586, Latvia

¹¹Tuorla Observatory, Department of Physics and Astronomy, University of Turku, Väisäläntie 20, FI-21500 Piikkiö, Finland

Subject headings: galaxies: active — QSOs: general

1. Introduction

QSOs are enigmatic objects in the Universe and due to their very high intrinsic luminosities they can be seen out to very large cosmological distances. Although great breakthroughs have come along since the first detection of quasi-stellar radio sources (Matthews & Sandage 1963, since then the term *QSO* or *quasar* has gained prevalence), many questions regarding their physical nature remain unsolved. In order to draw robust conclusions about the population of QSOs as a whole it is important to have a representative sample; however, most studies in the past have relied on colour selections of QSOs from large optical surveys, e.g., the Sloan Digital Sky Survey (SDSS, York et al. 2000) and the 2dF QSO redshift survey (Croom et al. 2004). Though any selection on colour inherently biases the selected sample, the power of colour selection lies in the ability to quickly build a large sample without investing large amounts of time on spectroscopic classification.

QSOs are thought to be transitional phenomena originating in the environments of super-massive black holes in the cores of galaxies. The QSO activity is triggered by mechanisms that cause material to be accreted onto the central black holes, e.g., mergers or hydrodynamical instabilities within the galaxies. Such major events are also believed to induce strong star formation activity leading to the formation of large amounts of dust. Some part of the population is thus expected to be found in dust-rich environments leading to red optical colours. The search for red QSOs has a long history (e.g., Benn et al. 1998; Warren et al. 2000; Gregg et al. 2002; Richards et al. 2003; Hopkins et al. 2004; Polletta et al. 2006; Lacy et al. 2007; Maddox et al. 2008; Urrutia et al. 2009; Banerji et al. 2012; Glikman et al. 2007, 2012, 2013; Maddox et al. 2012). The detection of red QSOs in most of these works relied on either radio or X-ray detections (see Warren et al. 2000, for an extensive discussion). Recently, large area surveys in the near-infrared have made it possible to select QSOs based on near-infrared photometry (Warren et al. 2007; Peth et al. 2011; Maddox et al. 2012) and this is the approach we have adopted in this work.

The red colours of QSOs may be caused by dust in intervening absorption systems as well. If the intervening absorber is very dust-rich it may cause reddening and dimming of the background QSO to the point where optical selection will fail at identifying the source as a QSO. A bias may therefore exist against very dusty and hence very metal-rich absorption systems leading to underestimation of the cosmic chemical abundance in absorption systems (Pontzen & Pettini 2009; Khare et al. 2012). In Fynbo et al. (2013, hereafter Paper I), we investigated the population of red QSOs missing in the SDSS DR7 sample, motivated by the discoveries of intervening absorbers causing reddening

¹Based on observations made with the Nordic Optical Telescope, operated on the island of La Palma jointly by Denmark, Finland, Iceland, Norway, and Sweden, in the Spanish Observatorio del Roque de los Muchachos of the Instituto de Astrofísica de Canarias.

of the background QSOs to the point where these QSOs were close to dropping out of the colour criteria invoked by SDSS-I/II (Noterdaeme et al. 2009b, 2010; Kaplan et al. 2010; Fynbo et al. 2011; Noterdaeme et al. 2012; Jian-Guo et al. 2012). Selecting candidate QSOs on basis of their near-infrared colours showed that indeed QSOs were missing in the SDSS DR7 sample of QSOs, see Paper I. Any bias in QSO samples affects both the study of the QSOs themselves, absorption features in the QSOs [e.g., broad absorption line (BAL) QSOs (Saturni et al. 2014, submitted)], and the samples of intervening absorption systems (Richards et al. 2003; Maddox et al. 2012).

In this work, we present revised criteria of those utilized in Paper I to target more reddened QSOs. The colour criteria allows us to select a pure (though not complete) sample of highly reddened QSO candidates. We here present and discuss our spectroscopic follow-up campaign, The High A(V) Quasar (HAQ) Survey. In Sect. 2, we present our selection criteria. In Sect. 3 and Sect. 4, we describe our observations and analysis of the HAQ sample. In Sect. 5, we discuss the implications of our work.

2. Photometric Data and Selection

2.1. Photometric data

The selection of candidate red QSOs is based purely on optical and near-infrared photometry. The photometry was selected from the overlap region between the SDSS data release 7 (u , g , r , i , and z bands) and the UKIRT Infrared Deep Sky Survey (Y , J , H , and K_s).

In our analysis, we also include data from the Wide-field Infrared Survey Explorer (WISE) providing photometry in four bands in the mid-infrared at 3.4, 4.6, 12, and 22 μm . In cases where the flux is detected at less than 2σ , we quote the flux in the given band as an upper limit.

2.2. Selection Criteria

Our aim is to look for this population of red QSOs, which is missed in the optical QSO samples, by using a set of colour selection criteria that were refined with respect to those of Paper I. By studying the distribution of colours (see Fig. 1) of the various identified targets in our pilot study, we find that we can significantly reduce the small fraction of contaminating galaxies and stars using these refined colour criteria (all on the AB magnitude system):

$$J - K > 0 ; H - K > 0 ; J - H < 0.4 ; 0.5 < g - r < 1.0 ; 0.1 < r - i < 0.7.$$

Moreover, the revised criteria also improve the selection of QSOs with redshifts in the range $2.5 < z < 3.5$, which were missing in the sample presented in Paper I. In total we have selected 901 point sources common to the SDSS and UKIDSS survey fields fulfilling these refined selection

criteria down to a flux limit of $J_{AB} < 19$. Of these, $\sim 45\%$ had already been observed by SDSS (DR8) and found to be QSOs (either dust reddened, BALs, or at $z \gtrsim 3$). From the remaining 492 targets without spectroscopy from SDSS, we selected our sample for spectroscopic follow-up.

In Fig. 1, we compare the selection criteria from Paper I with the refined criteria described above. We only show the criteria for $g - r$, $r - i$, and $J - K$ as these are the colours that both set of criteria have in common. As can be seen in Fig. 1, the two selections overlap in these two colour-spaces. In total there are 15 out of 58 objects from Paper I that also fulfil all the revised selection criteria. The targets from Paper I that were not spectroscopically classified as QSOs (i.e., stars and galaxies) are shown in Fig. 1 as black squares. Since these concentrate in a specific part of the colour-colour diagram shown in Fig. 1, we can effectively remove them by excluding these regions of colour space.

3. Spectroscopic Observations and Data Reduction

During a range of observing runs in 2012, 2013, and 2014, 159 candidate red QSOs were observed with the Nordic Optical Telescope (NOT) on La Palma, using the Andalucia Faint Object Spectrograph and Camera (ALFOSC). As in Paper I, we used grism #4, which covers the wavelength range from about 3200 Å to 9100 Å at a resolution of about 300 with a slit width of 1.3 arcsec. Redwards of about 7000 Å the spectra are strongly affected by fringing, which was alleviated by dithering along the slit. In order to prevent 2nd order contamination, a blocking filter was used for the observations with grism #4. We used filter no. #94 which blocks out wavelengths shorter than 3560 Å. The spectra were taken aligning the slit at the parallactic angle. In some cases of bad seeing, we observed with a 1.8 arcsec slit. Four sources (HAQ0047+0826, HAQ0151+1453, HAQ1115+0333, and HAQ2300+0914) were also observed with grism #6 which covers the wavelength range from about 3200 Å to 5500 Å at a resolution of about 500 with the 1.0 arcsec slit. For one target (HAQ1115+0333), we observed with grism #7 to look for intervening absorption. Grism #7 covers wavelengths from about 3850 Å to 6850 Å at a resolution of about 650 with the 1.0 arcsec slit. We binned the CCD pixels by a factor of 2 along the wavelength axis.

After the release of SDSS-DR9 in August 2012 we noted that 11 of the candidates, which we followed up, had been observed by SDSS. With the new release of DR10, the number of candidates with spectra from SDSS is now 25. For targets that were observed by the Baryon Oscillation Spectroscopic Survey (BOSS), we present the spectra from the NOT along with BOSS spectra. However, we preferentially use the BOSS spectra in our analysis if available, since they have larger wavelength coverage, higher signal to noise and better resolution ($R \sim 2000$) (Dawson et al. 2013). In Table 1, we give a full list of all the observed targets.

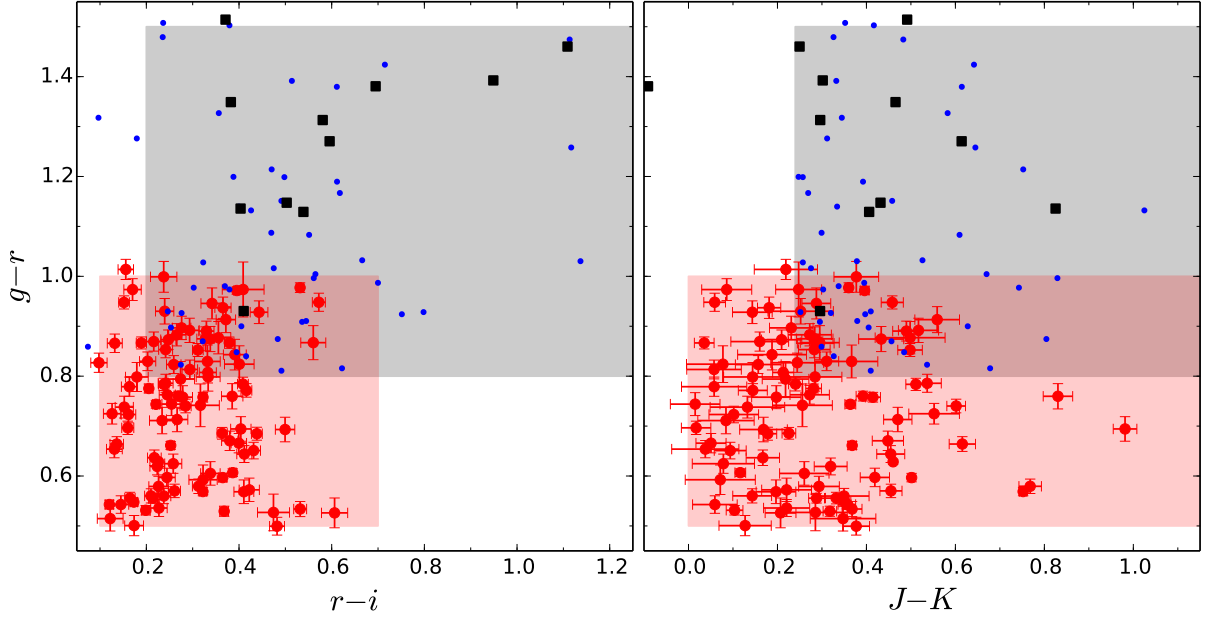


Fig. 1.— Comparison of the colour criteria used in this work (red region) to those from Fynbo et al. 2013 (Paper I) (gray region). The left and right panels show $g-r$ versus $r-i$ and $g-r$ versus $J-K$, respectively. The big, red points with error-bars represent the sample that we observed in this work. The small, blue points represent the sample from Paper I. As can be seen, there is a small overlap between the two criteria. Targets from Paper I that were *not* classified as QSOs are shown as black squares. These contaminants (galaxies and stars) are primarily concentrated in the upper part of the colour-colour diagrams. This distribution is part of the motivation for the revised criteria resulting in a higher efficiency of QSO selection.

The spectra were reduced using a combination of IRAF² and MIDAS³ tasks for low-resolution spectroscopy. Cosmic rays were rejected using the software written by van Dokkum (2001). The spectrophotometric standard star observed on the same night as the science spectra was used for the flux calibration. In order to improve the absolute flux-calibration, we scaled the spectra to the r -band photometry from SDSS. Finally, the spectra were corrected for Galactic extinction using the extinction maps from Schlegel et al. (1998).

²IRAF is distributed by the National Optical Astronomy Observatory, which is operated by the Association of Universities for Research in Astronomy (AURA) under cooperative agreement with the National Science Foundation.

³ESO-MIDAS is a copyright protected software product of the European Southern Observatory. The software is available under the GNU General Public License.

Table 1. Full sample observed with the NOT.

Target	RA (J 2000)	Dec (J 2000)	r_{SDSS} (mag)	Telescope	Exptime (sec)
HAQ 0000+0557	00 00 33.979	+05 57 53.77	19.75	NOT, BOSS	3×780
HAQ 0001+0233	00 01 21.685	+02 33 04.87	17.86	NOT	2×600
HAQ 0008+0835	00 08 15.020	+08 35 25.68	18.24	NOT	2×450
HAQ 0008+0846	00 08 25.327	+08 46 26.20	18.81	NOT	2×600
HAQ 0011+0122	00 11 04.665	+01 22 56.02	18.28	NOT	900
HAQ 0012+0651	00 12 55.339	+06 51 22.76	18.70	NOT	2×600
HAQ 0012+0657	00 12 43.499	+06 57 36.74	18.98	NOT	2×600
HAQ 0012+0944	00 12 01.587	+09 44 02.21	18.13	NOT	2×500
HAQ 0014+0444	00 14 05.324	+04 44 09.35	17.75	NOT	2×600
HAQ 0014+0939	00 14 13.425	+09 39 06.47	18.77	NOT, BOSS	2×600
HAQ 0015+0736	00 15 35.496	+07 36 37.54	19.09	NOT, BOSS	3×600
HAQ 0015+0811	00 15 31.492	+08 11 36.96	19.00	NOT	2×600
HAQ 0015+1129	00 15 22.046	+11 29 59.89	17.89	NOT	2×600
HAQ 0015+1340	00 15 58.255	+13 40 05.37	19.61	NOT	3×600
HAQ 0018+1133	00 18 25.423	+11 33 01.62	19.03	NOT	2×600
HAQ 0020+0259	00 20 20.401	+02 59 13.88	19.03	NOT	2×600
HAQ 0022+0147	00 22 24.417	+01 47 31.23	17.52	NOT	3×250
HAQ 0024+1037	00 24 06.099	+10 37 58.03	17.06	NOT	3×250
HAQ 0025+0220	00 25 10.345	+02 20 06.35	18.93	NOT	2×600
HAQ 0026+0640	00 26 12.462	+06 40 36.80	18.83	NOT	2×600
HAQ 0031+1328	00 31 16.660	+13 28 48.44	17.60	NOT	2×600, 300
HAQ 0033+0915	00 33 57.209	+09 15 53.66	19.23	NOT, BOSS	3×600
HAQ 0034+0950	00 34 28.096	+09 50 20.64	18.33	NOT	900
HAQ 0038+1426	00 38 06.431	+14 26 02.78	18.79	NOT	2×600
HAQ 0042+1220	00 42 15.000	+12 20 08.00	19.24	NOT	3×600
HAQ 0043+0549	00 43 16.644	+05 49 42.33	18.77	NOT	2×600
HAQ 0043+1136	00 43 28.876	+11 36 26.49	19.26	NOT	3×540
HAQ 0044+0817	00 44 30.382	+08 17 13.79	18.84	NOT, BOSS	3×400
HAQ 0044+1250	00 44 45.699	+12 50 19.86	19.17	NOT	2×900
HAQ 0045+1217	00 45 43.339	+12 17 11.83	17.43	NOT	3×400
HAQ 0046+0839	00 46 33.895	+08 39 13.78	19.71	NOT, BOSS	3×720
HAQ 0047+0826	00 47 37.196	+08 26 38.47	17.29	NOT	4×200

Table 1—Continued

Target	RA (J 2000)	Dec (J 2000)	r_{SDSS} (mag)	Telescope	Exptime (sec)
HAQ 0051+1542	00 51 54.685	+15 42 05.90	18.83	NOT	2×600
HAQ 0053+0216	00 53 36.998	+02 16 36.60	18.58	NOT	2×600
HAQ 0056+1132	00 56 45.104	+11 32 38.72	19.11	NOT	3×600
HAQ 0057+1155	00 57 31.960	+11 55 12.13	18.61	NOT	2×600
HAQ 0059+1238	00 59 48.164	+12 38 36.79	18.75	NOT	2×600
HAQ 0102+0249	01 02 16.770	+02 49 52.52	18.68	NOT	600
HAQ 0110+0303	01 10 13.499	+03 03 56.17	18.91	NOT	2×600
HAQ 0118+0323	01 18 13.583	+03 23 34.30	18.62	NOT	2×600
HAQ 0118+0700	01 18 57.315	+07 00 29.15	19.16	NOT, BOSS	2×600
HAQ 0119+0817	01 19 09.186	+08 17 53.87	19.08	NOT	2×900
HAQ 0120+0351	01 20 30.091	+03 51 46.88	18.95	NOT	3×480
HAQ 0121+0455	01 21 45.522	+04 55 04.50	18.16	NOT	2×900
HAQ 0122+0325	01 22 09.876	+03 25 43.64	17.87	NOT	600
HAQ 0130+1439	01 30 16.520	+14 39 53.71	19.93	NOT	4×600
HAQ 0138+0124	01 38 02.071	+01 24 24.47	18.26	NOT, BOSS	2×600
HAQ 0138+0636	01 38 19.887	+06 36 36.05	18.92	NOT	2×600
HAQ 0143+1509	01 43 17.885	+15 09 15.41	19.35	NOT	2×1000
HAQ 0151+0618	01 51 36.733	+06 18 31.67	19.16	NOT	3×600
HAQ 0151+1453	01 51 57.714	+14 53 08.34	19.53	NOT	3×360
HAQ 0155+0438	01 55 03.728	+04 38 30.42	18.38	NOT	900
HAQ 0201+0223	02 01 14.291	+02 23 33.29	19.07	NOT	1080
HAQ 0204+0327	02 04 58.663	+03 27 03.22	18.55	NOT	2×600
HAQ 0206+0624	02 06 14.665	+06 24 54.44	19.01	NOT	2×600
HAQ 0208+0521	02 08 15.802	+05 21 06.01	19.10	NOT	2×900
HAQ 0211+1214	02 11 23.395	+12 14 01.20	18.32	NOT	2×600
HAQ 0226+0729	02 26 50.310	+07 29 52.78	19.06	NOT	2×900
HAQ 0236+0619	02 36 46.962	+06 19 03.15	19.03	NOT	2×600
HAQ 0243+0355	02 43 29.118	+03 55 59.50	17.84	NOT	3×240
HAQ 0318+0424	03 18 16.302	+04 24 06.35	19.50	NOT	5×400
HAQ 0318+0434	03 18 33.519	+04 34 43.48	19.20	NOT	1500
HAQ 0319+0623	03 19 01.776	+06 23 39.04	18.92	NOT	4×450
HAQ 0329+0553	03 29 15.624	+05 53 39.57	18.92	NOT	2×600

Table 1—Continued

Target	RA (J 2000)	Dec (J 2000)	r_{SDSS} (mag)	Telescope	Exptime (sec)
HAQ 0329+0609	03 29 09.017	+06 09 14.30	19.14	NOT	4×500
HAQ 0337+0539	03 37 38.075	+05 39 10.95	18.18	NOT	2×600
HAQ 0339+0420	03 39 30.630	+04 20 31.11	18.75	NOT	4×360
HAQ 0340+0408	03 40 14.148	+04 08 31.94	19.36	NOT	4×600
HAQ 0345−0009	03 45 50.472	−00 09 07.56	18.53	NOT	4×375
HAQ 0347+0115	03 47 48.060	+01 15 44.52	19.06	NOT	2×600
HAQ 0355−0025	03 55 52.570	−00 25 04.22	18.70	NOT	4×400
HAQ 0355−0053	03 55 46.908	−00 53 39.83	19.46	NOT	2×780
HAQ 1106+0300	11 06 12.667	+03 00 49.10	17.62	NOT	3×300
HAQ 1114+1330	11 14 15.151	+13 30 59.64	17.59	NOT	3×400
HAQ 1115+0333	11 15 49.737	+03 33 51.35	18.89	NOT	3×600
HAQ 1148−0117	11 48 22.193	−01 17 29.20	18.02	NOT	2×500, 3×400
HAQ 1207+1341	12 07 59.229	+13 41 15.28	18.40	NOT	3×500
HAQ 1233+1304	12 33 55.605	+13 04 09.21	17.71	NOT	3×250
HAQ 1247+3403	12 47 02.054	+34 03 58.17	18.36	NOT, BOSS	2×500
HAQ 1248+2951	12 48 48.423	+29 51 06.73	18.19	NOT	2×400
HAQ 1315+0440	13 15 21.006	+04 40 00.56	18.70	NOT	3×500
HAQ 1319+3214	13 19 02.712	+32 14 51.29	19.50	NOT	4×600
HAQ 1327+3206	13 27 57.361	+32 06 50.63	18.55	NOT	2×600
HAQ 1332+0052	13 32 54.515	+00 52 50.63	18.35	NOT, BOSS	2×600
HAQ 1339+3331	13 39 41.381	+33 31 12.64	18.57	NOT	1200
HAQ 1355+3407	13 55 57.499	+34 07 39.03	18.77	NOT	2×800
HAQ 1358+2401	13 58 59.897	+24 01 07.00	18.86	NOT	2×900
HAQ 1400+0219	14 00 47.108	+02 19 34.80	19.81	NOT	4×600
HAQ 1409+0940	14 09 52.589	+09 40 23.73	19.65	NOT, BOSS	3×600
HAQ 1411−0104	14 11 59.671	−01 04 42.60	19.28	NOT	3×600
HAQ 1434+0448	14 34 15.006	+04 48 46.83	19.77	NOT	4×750
HAQ 1444+0752	14 44 43.539	+07 52 24.28	19.45	NOT, BOSS	3×600, 5×750
HAQ 1451+3239	14 51 56.221	+32 39 51.69	19.09	NOT	2×600
HAQ 1506+0438	15 06 29.847	+04 38 44.27	19.97	NOT	4×600
HAQ 1509+1214	15 09 53.554	+12 14 44.98	18.54	NOT, BOSS	2×600
HAQ 1517+0817	15 17 55.714	+08 17 27.66	19.15	NOT	2×600

Table 1—Continued

Target	RA (J 2000)	Dec (J 2000)	r_{SDSS} (mag)	Telescope	Exptime (sec)
HAQ 1524–0053	15 24 44.652	–00 53 09.70	19.50	NOT	3×600
HAQ 1527+0250	15 27 10.942	+02 50 19.20	17.06	NOT	5×200
HAQ 1534+0013	15 34 52.677	+00 13 17.71	18.82	NOT	2×600
HAQ 1535+0157	15 35 53.854	+01 57 11.36	18.86	NOT	2×600
HAQ 1545–0130	15 45 49.013	–01 30 09.26	19.34	NOT	3×600
HAQ 1546+0005	15 46 58.586	+00 05 38.33	19.01	NOT, BOSS	2×750
HAQ 1600+2911	16 00 33.974	+29 11 16.46	19.82	NOT	4×900
HAQ 1603+2512	16 03 28.589	+25 12 14.33	20.18	NOT	2×1350
HAQ 1606+2902	16 06 01.112	+29 02 18.85	19.58	NOT	4×600
HAQ 1606+2903	16 06 28.064	+29 03 33.80	17.53	NOT, BOSS	3×480
HAQ 1607+2611	16 07 21.764	+26 11 07.06	19.67	NOT	4×600
HAQ 1611+2453	16 11 41.495	+24 53 22.21	19.69	NOT	3×600
HAQ 1620+2955	16 20 40.932	+29 55 06.56	19.21	NOT, BOSS	1200
HAQ 1626+2517	16 26 21.102	+25 17 14.00	19.33	NOT, BOSS	2×1000
HAQ 1633+2851	16 33 50.413	+28 51 56.77	19.45	NOT	2×900
HAQ 1634+2811	16 34 39.605	+28 11 38.28	19.25	NOT	2×900
HAQ 1639+3157	16 39 57.963	+31 57 26.71	19.60	NOT, BOSS	3×600
HAQ 1643+2944	16 43 32.810	+29 44 23.42	19.48	NOT	3×600
HAQ 1645+3056	16 45 53.184	+30 56 07.27	19.14	NOT, BOSS	3×600
HAQ 1645+3130	16 45 47.802	+31 30 03.28	19.50	NOT, BOSS	3×600
HAQ 1655+3051	16 55 23.891	+30 51 37.71	19.38	NOT	3×600
HAQ 2159+0212	21 59 36.617	+02 12 33.51	18.73	NOT	600, 2×600
HAQ 2203–0052	22 03 08.631	–00 52 34.54	19.05	NOT	2×900
HAQ 2217+0359	22 17 40.515	+03 59 33.78	19.43	NOT	2×900
HAQ 2221+0145	22 21 43.557	+01 45 37.37	19.05	NOT, BOSS	2×600
HAQ 2222+0604	22 22 06.684	+06 04 15.71	19.38	NOT	2×900
HAQ 2225+0527	22 25 14.695	+05 27 09.10	18.11	NOT	2×600, 2×450
HAQ 2229+0324	22 29 15.168	+03 24 52.71	19.90	NOT, BOSS	3×600
HAQ 2231+0509	22 31 15.996	+05 09 48.62	19.10	NOT	2×900
HAQ 2241+0818	22 41 51.844	+08 18 59.09	19.06	NOT	2×900
HAQ 2244+0335	22 44 53.750	+03 35 23.29	18.66	NOT, BOSS	2×600
HAQ 2245+0457	22 45 28.459	+04 57 20.38	18.32	NOT	2×600, 2×600

Table 1—Continued

Target	RA (J 2000)	Dec (J 2000)	r_{SDSS} (mag)	Telescope	Exptime (sec)
HAQ 2246+0710	22 46 03.823	+07 10 50.92	18.02	NOT	2×600
HAQ 2247+0146	22 47 20.277	+01 46 04.95	19.18	NOT	5×600
HAQ 2252+0434	22 52 45.969	+04 34 36.75	16.03	NOT	4×90
HAQ 2253+1141	22 53 30.058	+11 41 18.31	19.20	NOT	2×600
HAQ 2254+0638	22 54 32.268	+06 38 26.01	18.41	NOT	600
HAQ 2300+0914	23 00 56.010	+09 14 03.85	18.86	NOT	2×600
HAQ 2301+0832	23 01 22.475	+08 32 01.43	17.26	NOT	2×600
HAQ 2303+0238	23 03 17.785	+02 38 09.60	18.75	NOT	2×600
HAQ 2303+0630	23 03 12.032	+06 30 14.21	18.67	NOT	2×600
HAQ 2305+0117	23 05 48.832	+01 17 41.63	19.55	NOT	3×650
HAQ 2310+1117	23 10 46.942	+11 17 21.55	20.06	NOT	4×600
HAQ 2311+1444	23 11 38.547	+14 44 36.72	19.18	NOT, SDSS	3×600
HAQ 2313+0955	23 13 34.552	+09 55 00.03	18.91	NOT	2×600
HAQ 2318+0255	23 18 12.807	+02 55 38.98	18.31	NOT	2×600
HAQ 2326+0642	23 26 48.823	+06 42 35.96	18.79	NOT	2×600
HAQ 2326+1423	23 26 40.965	+14 23 03.37	19.02	NOT	2×450
HAQ 2330+1009	23 30 59.933	+10 09 49.42	19.19	NOT	3×500
HAQ 2333+0113	23 33 35.516	+01 13 29.32	19.85	NOT, BOSS	4×900
HAQ 2333+0619	23 33 11.434	+06 19 31.18	19.31	NOT	2×900
HAQ 2335+1407	23 35 12.070	+14 07 31.56	19.71	NOT	4×600
HAQ 2337+1343	23 37 18.332	+13 43 06.02	19.00	NOT	2×600
HAQ 2339+1232	23 39 38.008	+12 32 01.49	18.40	NOT	2×600
HAQ 2340+0121	23 40 54.272	+01 21 41.34	18.81	NOT	2×600
HAQ 2343+0615	23 43 44.229	+06 15 00.60	19.39	NOT	3×600
HAQ 2348+0716	23 48 44.464	+07 16 58.34	18.49	NOT	900
HAQ 2351+1429	23 51 06.509	+14 29 39.41	20.12	NOT	4×750
HAQ 2352+0105	23 52 38.088	+01 05 52.35	17.33	NOT, BOSS	4×225
HAQ 2358+0339	23 58 33.476	+03 39 55.79	17.91	NOT	2×300
HAQ 2358+0359	23 58 16.016	+03 59 44.69	19.95	NOT	4×600
HAQ 2358+0520	23 58 46.404	+05 20 52.00	19.47	NOT	3×600
HAQ 2358+1436	23 58 19.661	+14 36 42.03	19.45	NOT	3×600

4. Results

In Fig. 2, we show the 1-dimensional spectra of all targets in our sample along with the photometry from SDSS and UKIDSS. We are able to securely identify 154 out of 159 targets as QSOs. Two remain unidentified, only two objects are identified as stars, and one is most probably a BL Lacertae object (Stein et al. 1976). We thus have a purity (or efficiency) of $P \sim 97\%$, defined as the ratio of QSOs to total objects in the sample. In Table 2, we present the identification of all objects, their radio flux from FIRST, and an estimate of the extinction assuming Small Magellanic Cloud (SMC) type dust at the redshift of the QSO unless specified otherwise. Only three QSOs in our sample were flagged as QSO candidates by SDSS. These are marked with the SDSS-flag ‘QSO_HIZ’ or ‘QSO_CAP’ in Table 2. In the notes of Table 2, we give the redshift inferred by BOSS for the cases with BOSS spectra, along with remarks on available spectra observed with other grisms, e.g., Grism #6 or #7.

4.1. Confirmed QSOs

As in Paper I, the redshifts have been determined by the emission lines visible in the spectra. We estimate the extinction of each QSO by fitting a QSO template to the photometry and spectrum combined. Spectral regions that are influenced by strong emission and absorption lines are masked out in the fit. We use, as in Paper I, a combined template from Vanden Berk et al. (2001) and Glikman et al. (2006). We disregard photometric points on the blue side of the Ly- α emission line, upper limits, and data points influenced by strong absorption (especially in case of broad absorption lines). Furthermore, we always exclude the r -band from the fit since this band has been used to scale the spectra to match the photometry. In order to test whether we primarily observe signs of dust in the QSO itself or dust along the line-of-sight, we fit two sets of models: one model assuming that the dust is located in the QSO host galaxy (the null hypothesis) and another model allowing both dust in the QSO and in an intervening absorption system (the general model). Furthermore, we run each set of models for two different reddening laws, Small Magellanic Cloud (SMC) and Large Magellanic Cloud (LMC) as parametrized by Gordon et al. (2003) with a modification for wavelengths greater than 4400 Å (see Fitzpatrick & Massa 2005). The model we fit can be summarized as follows:

$$F_{\text{obs}} = C \cdot F_0 \cdot \exp \left(-\frac{1}{2.5 \log(e)} [A(V) \cdot k_{\text{QSO}} + A(V)_{\text{abs}} \cdot k_{\text{abs}}] \right),$$

where F_0 denotes the rest-frame QSO template before reddening is applied, F_{obs} refers to the reddened template, and $A(V)$ is the amount of extinction applied in the QSO’s rest frame given the reddening law, k_{QSO} . We assume that the dust in the QSO is SMC type (e.g., Hopkins et al. 2004). Likewise, $A(V)_{\text{abs}}$ denotes the amount of extinction applied in the putative absorber’s rest-frame at z_{abs} given the reddening law for the absorber, k_{abs} (SMC or LMC). C is an arbitrary scale factor, since we do not know the intrinsic flux of the QSO before reddening is applied. The null hypothesis

can then be constructed by restricting the extinction and redshift for the absorber in the general model: $A(V)_{\text{abs}} = z_{\text{abs}} = 0$. This nested nature of the models allows us to use a likelihood ratio test to compare the two models.

For a given reddened template, F_{obs} , we calculate synthetic fluxes for the template in each photometric band, weighted by the appropriate filter transmission curve. Next, we interpolate the template onto the wavelength grid of the observed spectrum thereby creating a "model spectrum", which can be directly compared to the observed spectrum. For the fitting, we re-bin the spectra by a factor of two to decrease the influence of noise. We calculate the residuals using both the spectroscopic and photometric data available for each given object. The fit is then performed using χ^2 minimization utilizing a Levenburg-Marquardt algorithm as implemented in the Python package `lmfit`⁴. For the null hypothesis, we keep the absorber parameters fixed ($A(V)_{\text{abs}} = z_{\text{abs}} = 0$) and only fit the remaining two parameters: the extinction at the QSO redshift, $A(V)$, and the scale factor, C . The parameter $A(V)$ is restricted to values larger than $A(V) > -0.2$. The inclusion of negative values of $A(V)$ takes into account any possible variation in the intrinsic slope of the QSO spectra. A negative value of $A(V)$ occurs if the QSO slope is intrinsically steeper than the template and no or little dust is present in the QSO. The limit of $A(V) > -0.2$ is motivated by the spread in $g - r$ color distribution of QSOs from Richards et al. (2001, see their fig. 8). The assumption that steeper QSO UV slopes can be approximated by including negative $A(V)$ values relies on the fact that, to first order, the SMC extinction law itself is a power-law (valid to within an error of $\lesssim 5\%$).

For the general model, we allow z_{abs} and $A(V)_{\text{abs}}$ to vary as well, however, the extinction at the absorber redshift is restricted to $A(V)_{\text{abs}} > 0$, since a negative extinction in the absorber is non-physical. Moreover, the absorber redshift is restricted to be $0 < z_{\text{abs}} < z_{\text{QSO}}$. We stress that when referring to the null hypothesis we quote the amount of extinction in the QSO rest-frame as just $A(V)$; however, in order to avoid confusion when referring to the general model, we quote the amount of extinction in the QSO rest-frame and absorber rest-frame as $A(V)_{\text{QSO}}$ and $A(V)_{\text{abs}}$, respectively.

⁴Written by Matthew Newville. Full documentation available at: <http://cars9.uchicago.edu/software/python/lmfit/>

Fig. Set 2. The spectra

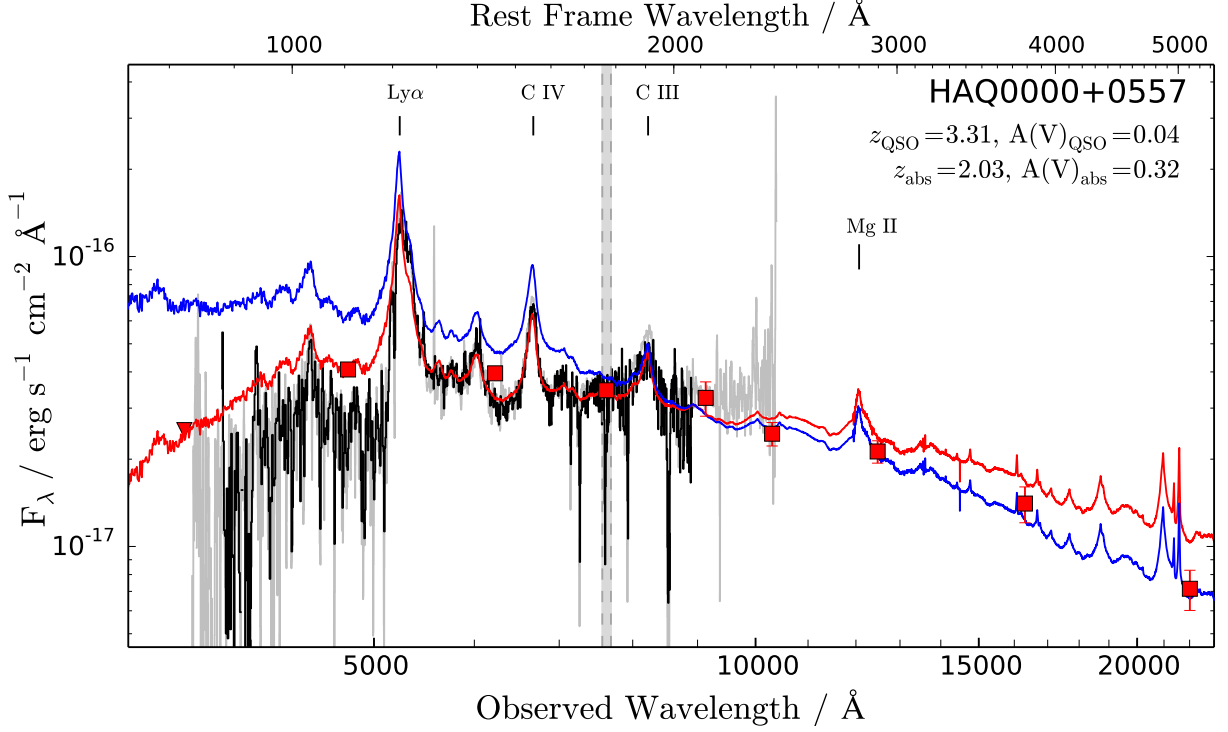


Fig. 2.— The observed spectrum is plotted as a solid black line. For targets observed with both grism 4 and 6, we show both the grism 4 and grism 6 spectra. In case of available SDSS data the spectrum from SDSS is shown in grey. In the upper right corner, the estimated emission redshift and rest-frame V -band extinction are provided. The unreddened composite QSO spectrum is shown in blue, redshifted to the spectroscopic redshift, and in red we show the redshifted composite spectrum reddened by the indicated amount of extinction. Overplotted with filled squares are the SDSS and UKIDSS photometric data points. The NOT spectra have been scaled to match the r -band photometric data point from SDSS. Unless otherwise noted we have assumed an SMC-like extinction curve. Note that the spectra have not been corrected for telluric absorption (marked with a grey band at ~ 7600 Å). (The full set of figures is available on the survey webpage <http://www.dark-cosmology.dk/~krogager/redQSOs/data.html>)

4.1.1. Model Comparison

In order to evaluate whether the general model with dust in an intervening system provides a significantly better fit we use a likelihood ratio test. This test quantifies how likely the observed improvement is, given the added free parameters. The logarithmic likelihood ratio is defined as $L = -2 \ln(\Lambda_0/\Lambda_G)$, where Λ_0 and Λ_G are the likelihoods for the null hypothesis and the general model, respectively. This can be simplified in our case since we assume that our uncertainties are Gaussian. In this case, $\chi^2 = -2 \ln(\Lambda)$ is a direct measure of the logarithmic likelihood. We thus get: $L = \chi_0^2 - \chi_G^2$, where χ_0^2 and χ_G^2 are the χ^2 of the best fit for the null model and the general model, respectively. The ratio, L , will be distributed approximately as a χ^2 distribution with number of degrees of freedom, ν , given by the change in degrees of freedom between the two models, which is equal to the change in number of parameters ($\Delta\nu = 2$). For each set of models for a given dataset, we can then calculate the chance probability of encountering the calculated change in χ^2 given the addition of two extra free parameters. This is the so-called p -value. In order to reject the null hypothesis, i.e., preferring a model with dust in the intervening system, we use a 5σ level significance, hence the p -value must be less than $p < 5.7 \cdot 10^{-7}$. For a χ^2 distribution with $\nu = 2$ this corresponds to a threshold of $L > 28.75$. The change in χ^2 must therefore be larger than 28.75 in order to reject the null hypothesis. We use such a strict criterion since the reddening estimates are very degenerate when introducing a second reddening system. Moreover, we require that the fit with intervening absorption (the general model) provides a *good* fit, since a model which to begin with provides a bad fit easily can improve significantly in terms of χ^2 when adding two free parameters but still provide a bad fit.

For a model to provide a good fit to the data, the distribution of normalized residuals⁵ should be normally distributed, i.e., follow a Gaussian distribution of $\mu = 0$ and $\sigma^2 = 1$. We subsequently use a Kolmogorov-Smirnov (KS) test to check the departure of the normalized residuals from normality. The one-sample KS test measures the difference between the cumulative distribution of the test sample and that of a normal distribution. One can then assign a probability (P_{KS}) of encountering at least this difference given the hypothesis that the test sample is drawn from a normal distribution. Hence a high value of P_{KS} means that the test sample is consistent with being drawn from a normal distribution. For our purpose, we require that the distribution of normalized residuals have $P_{KS} > 0.1$, i.e., at the 10% confidence level, we have no probabilistic evidence against the hypothesis that the residuals are normally distributed. Finally, we disregard fits where one or more parameters have reached the limit of the allowed range, thus not giving a fully converged fit. We do not use the simple reduced χ^2 as estimator for goodness-of-fit, since the minimization problem is non-linear; therefore, the exact number of degrees of freedom for each model is not well-determined. The change in number of degrees of freedom, however, is.

For the model fits assuming SMC type dust in the absorber, we find no evidence for improved

⁵also sometimes referred to as standardized residuals: $(\mu - x)/\sigma$, where μ , x , and σ denote, respectively, model, data, and uncertainty.

fits when including intervening dusty absorbers. However, when assuming that the dust in the absorber is LMC type we find 9 QSOs for which the model with intervening dust is preferred. The best-fit parameters for these 9 QSOs are given in Table 3. In all other cases where the null hypothesis is preferred, we list the extinction, $A(V)$, at the QSO redshift assuming SMC type dust in Table 2. In Appendix A, we present a table with all the details for the cases with significant evidence for dust in an intervening system. The table shows the best-fit parameters to both the null model and the general model along with the resulting χ^2 for each model. Furthermore, we give the P_{KS} -value from the KS-test to the normalized residuals for each model. Finally, we give the overall p -value, i.e., the chance probability of the observed improvement (in terms of χ^2) given the extra free parameters. The uncertainties on the fit parameters for the general model have been obtained by using a Markov chain Monte Carlo method in order to get a robust evaluation of the confidence intervals. Details on the Monte Carlo simulations are given in Appendix A. Two of these 9 cases are shown in Fig. 3 to demonstrate the improvement of the fit when including intervening dust. The remaining cases are shown in Appendix D.

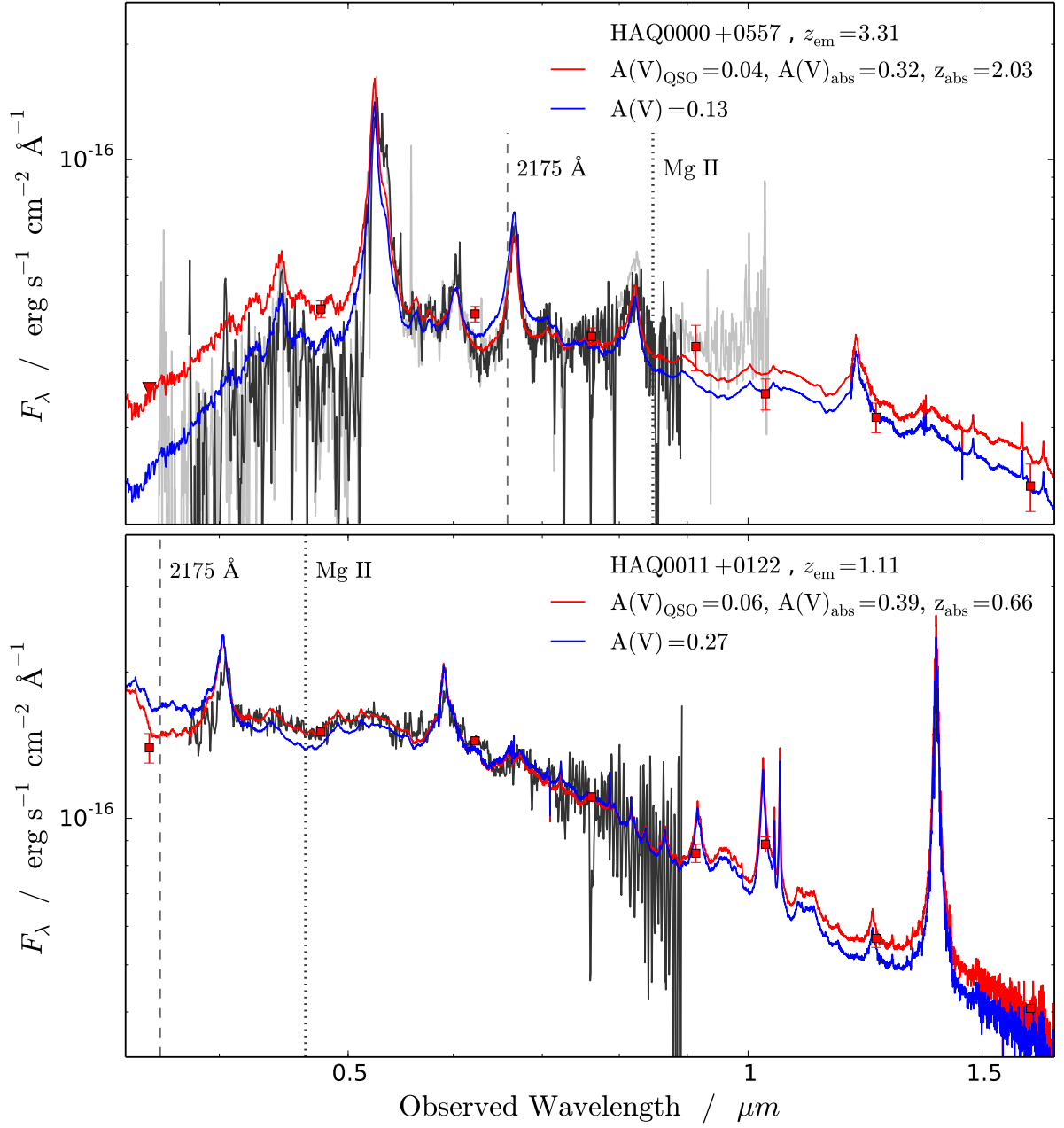


Fig. 3.— Spectra and photometry for two of the QSOs with evidence for dust in an intervening absorption system. Each panel shows the NOT spectrum in black and the SDSS and UKIDSS photometry as red squares. The blue and red templates show the best-fit null model and general model, respectively (see text for definition). In the top panel, the underlying gray spectrum is the SDSS spectrum which has been smoothed with a 3-pixel Gaussian kernel for presentation purposes. The dashed and dotted vertical lines indicate the locations of the 2175 \AA bump and Mg II at the best-fit redshift for the absorber.

Table 2. Results of the spectroscopic follow-up.

Target	Type	z_{QSO}	A(V)	$F_{1.4\text{GHz}}$ mJy	Notes
HAQ 0000+0557	QSO	3.31	0.32 ^(a)	< 0.34	(BOSS: $z=3.31$)
HAQ 0001+0233	QSO	1.89	0.06	< 0.40	
HAQ 0008+0835	QSO	1.19	0.00	< 0.31	
HAQ 0008+0846	QSO	1.23	0.04	< 0.36	
HAQ 0011+0122	QSO	1.11	0.39 ^(a)	5.03±0.14	
HAQ 0012+0651	QSO	1.12	0.36	< 0.39	
HAQ 0012+0657	QSO	2.43	0.00	< 0.39	
HAQ 0012+0944	QSO	2.03	0.00	< 0.39	
HAQ 0014+0444	QSO	1.05	0.48	< 0.36	
HAQ 0014+0939	QSO	3.19	0.00	< 0.39	(BOSS: $z=3.23$)
HAQ 0015+0736	QSO	3.63	−0.05	< 0.39	(BOSS: $z=3.67$)
HAQ 0015+0811	QSO	2.43	0.16	< 0.35	
HAQ 0015+1129	QSO	0.87	0.78	1.64±0.16	
HAQ 0015+1340	QSO	3.11	0.14	1.64±0.16	
HAQ 0018+1133	QSO	1.90	0.18	< 0.46	
HAQ 0020+0259	QSO	2.47	0.15	< 0.40	
HAQ 0022+0147	QSO	1.15	0.27	< 0.33	
HAQ 0024+1037	QSO	1.22	0.27	0.77±0.15	
HAQ 0025+0220	QSO	2.04	0.39	< 0.37	
HAQ 0026+0640	QSO	1.20	0.22	< 0.36	
HAQ 0031+1328	QSO	1.02	0.35 ^(a)	< 0.36	
HAQ 0033+0915	QSO	3.28	0.00	< 0.38	(BOSS: $z=3.31$)
HAQ 0034+0950	QSO	0.28	0.51	< 0.36	
HAQ 0038+1426	QSO	2.55	0.00	< 0.49	
HAQ 0042+1220	QSO	2.56	0.00	< 0.42	
HAQ 0043+0549	QSO	1.22	0.47	< 0.33	
HAQ 0043+1136	QSO	3.32	0.00	< 0.41	
HAQ 0044+0817	QSO	3.35	0.00	< 0.26	(BOSS: $z=3.31$)
HAQ 0044+1250	QSO	2.35	0.25	< 0.26	
HAQ 0045+1217	BL Lac	83.81±0.15	
HAQ 0046+0839	QSO	2.85	0.28	< 0.35	(BOSS: $z=2.84$)
HAQ 0047+0826	QSO	1.95	0.18	< 0.35	Grism 6

Table 2—Continued

Target	Type	z_{QSO}	A(V)	$F_{1.4\text{GHz}}$ mJy	Notes
HAQ 0051+1542	QSO	1.90	0.39 ^(a)	< 0.35	
HAQ 0053+0216	QSO	0.99	0.71	< 0.36	
HAQ 0056+1132	QSO	3.57	0.00	< 0.48	
HAQ 0057+1155	QSO	0.60	1.20	< 0.47	
HAQ 0059+1238	QSO	3.50	0.00	< 0.43	
HAQ 0102+0249	QSO	3.49	0.01	< 0.37	
HAQ 0110+0303	QSO	3.50	0.00	< 0.41	
HAQ 0118+0323	QSO	2.16	0.09	< 0.33	
HAQ 0118+0700	QSO	3.50	0.00	< 0.34	(BOSS: z=3.50)
HAQ 0119+0817	QSO	1.95	0.22	< 1.14	
HAQ 0120+0351	QSO	3.09	0.00	< 0.34	
HAQ 0121+0455	QSO	0.84	0.77	< 0.34	
HAQ 0122+0325	QSO	2.10	0.04	< 0.64	
HAQ 0130+1439	QSO	1.84	0.40	< 0.64	
HAQ 0138+0124	QSO	2.53	0.00	< 0.45	(BOSS: z=2.61)
HAQ 0138+0636	QSO	1.80	0.09	< 0.40	
HAQ 0143+1509	QSO	3.76	0.00	< 0.40	
HAQ 0151+0618	QSO	0.95	0.72	20.23±0.16	
HAQ 0151+1453	QSO	1.18	0.05	20.23±0.16	Grism 6
HAQ 0155+0438	QSO	1.13	0.46	167.63±0.29	
HAQ 0201+0223	QSO	2.24	0.19	165.22±0.10	
HAQ 0204+0327	QSO	0.83	0.66	7.53±0.13	
HAQ 0206+0624	QSO	1.20	0.83	1.57±0.13	
HAQ 0208+0521	QSO	1.07	0.40	< 0.37	Grism 6
HAQ 0211+1214	QSO	2.11	0.05	< 0.37	
HAQ 0226+0729	QSO	2.21	0.25	< 0.52	
HAQ 0236+0619	QSO	2.43	0.12	< 0.46	
HAQ 0243+0355	QSO	3.30	0.00	< 0.33	
HAQ 0318+0424	QSO	3.06	0.14	< 0.42	
HAQ 0318+0434	QSO	2.38	0.00	< 0.54	
HAQ 0319+0623	QSO	2.10	0.13	< 0.51	
HAQ 0329+0553	QSO	1.11	0.15	23.72±0.24	

Table 2—Continued

Target	Type	z_{QSO}	A(V)	$F_{1.4\text{GHz}}$ mJy	Notes
HAQ 0329+0609	QSO	1.44	0.00	23.72 ± 0.24	
HAQ 0337+0539	QSO	3.28	0.03	7.73 ± 0.15	
HAQ 0339+0420	QSO	1.80	$0.44^{(a)}$	1.28 ± 0.14	
HAQ 0340+0408	QSO	1.62	0.13	< 0.41	
HAQ 0345–0009	QSO	1.77	0.18	< 0.41	
HAQ 0347+0115	QSO	0.99	0.40	< 0.40	
HAQ 0355–0025	QSO	1.07	0.00	< 0.40	
HAQ 0355–0053	QSO	2.15	0.00	< 0.40	
HAQ 1106+0300	QSO	0.73	1.29	< 0.41	
HAQ 1114+1330	QSO	1.10	0.00	< 0.43	
HAQ 1115+0333	QSO	3.10	0.15	< 0.45	Grism 7
HAQ 1148–0117	QSO	2.70	0.12	< 0.45	
HAQ 1207+1341	QSO	2.37	0.12	< 0.41	
HAQ 1233+1304	QSO	2.34	0.02	< 0.44	
HAQ 1247+3403	QSO	1.18	0.48	< 0.43	(BOSS: $z=1.17$)
HAQ 1248+2951	QSO	3.55	$0.20^{(a)}$	< 0.41	
HAQ 1315+0440	QSO	2.17	0.13	< 0.43	
HAQ 1319+3214	QSO	3.50	0.00	< 0.42	
HAQ 1327+3206	QSO	2.48	0.01	< 1.64	
HAQ 1332+0052	QSO	3.52	0.05	< 0.41	(BOSS: $z=3.51$)
HAQ 1339+3331	QSO	3.40	0.00	< 0.41	
HAQ 1355+3407	QSO	3.16	0.00	< 0.44	
HAQ 1358+2401	QSO	3.40	0.03	< 0.41	
HAQ 1400+0219	QSO	0.86	0.85	< 0.46	
HAQ 1409+0940	QSO	0.92	0.93	< 0.44	(BOSS: $z=0.93$)
HAQ 1411–0104	QSO	3.50	0.00	< 0.44	
HAQ 1434+0448	QSO	1.20	0.57	< 0.45	
HAQ 1444+0752	QSO	2.42	0.05	6.17 ± 0.14	(BOSS: $z=2.45$)
HAQ 1451+3239	QSO	3.55	0.00	< 0.41	
HAQ 1506+0438	QSO	1.04	0.61	< 0.44	
HAQ 1509+1214	QSO	2.80	$0.45^{(a)}$	< 0.45	(BOSS: $z=2.89$)
HAQ 1517+0817	QSO	0.66	0.57	< 0.40	

Table 2—Continued

Target	Type	z_{QSO}	A(V)	$F_{1.4\text{GHz}}$ mJy	Notes
HAQ 1524–0053	G-dwarf	0.00	0.60	< 0.40	MW type dust
HAQ 1527+0250	QSO	2.13	0.20	< 0.81	
HAQ 1534+0013	QSO	3.44	0.00	< 0.42	
HAQ 1535+0157	QSO	3.12	0.17	< 0.44	
HAQ 1545–0130	QSO	3.49	0.00	< 0.44	
HAQ 1546+0005	QSO	3.61	0.00	< 0.77	(BOSS: $z=3.61$)
HAQ 1600+2911	QSO	2.00	0.41	< 0.43	
HAQ 1603+2512	QSO	1.92	0.55	< 0.41	
HAQ 1606+2902	QSO	1.82	0.25	< 0.44	
HAQ 1606+2903	QSO_CAP	0.43	0.72	< 0.45	(BOSS: $z=0.43$)
HAQ 1607+2611	Unknown	< 0.43	
HAQ 1611+2453	QSO	0.78	0.78	< 0.45	
HAQ 1620+2955	QSO	3.36	0.11	< 0.43	(BOSS: $z=3.36$)
HAQ 1626+2517	QSO	1.25	0.30	6.72 ± 0.14	(BOSS: $z=1.26$)
HAQ 1633+2851	QSO	1.14	0.52	< 0.43	
HAQ 1634+2811	QSO	2.60	0.10	< 0.39	
HAQ 1639+3157	QSO	0.81	0.79	< 0.41	(BOSS: $z=0.81$)
HAQ 1643+2944	QSO	1.08	0.44	< 0.45	
HAQ 1645+3056	QSO	2.50	0.10	< 0.41	(BOSS: $z=2.53$)
HAQ 1645+3130	QSO	0.93	0.69	< 0.40	(BOSS: $z=0.93$)
HAQ 1655+3051	QSO	1.27	0.53	< 0.43	
HAQ 2159+0212	QSO	1.26	0.10	< 0.37	
HAQ 2203–0052	QSO	1.24	$0.74^{(a)}$	< 0.37	
HAQ 2217+0359	QSO	0.98	0.52	< 0.37	
HAQ 2221+0145	QSO	3.43	$0.17^{(a)}$	< 0.37	(BOSS: $z=3.43$)
HAQ 2222+0604	QSO	2.45	0.25	< 0.46	
HAQ 2225+0527	QSO	2.32	0.29	882.52 ± 0.11	Grism 7
HAQ 2229+0324	QSO	2.64	0.28	< 0.40	(BOSS: $z=2.66$)
HAQ 2231+0509	QSO	1.76	0.35	< 0.40	
HAQ 2241+0818	QSO	2.43	0.04	< 0.33	
HAQ 2244+0335	QSO	3.37	0.00	< 0.37	(BOSS: $z=3.36$)
HAQ 2245+0457	QSO	2.10	0.12	< 0.36	

Table 2—Continued

Target	Type	z_{QSO}	A(V)	$F_{1.4\text{GHz}}$ mJy	Notes
HAQ 2246+0710	QSO	1.20	0.12	< 0.37	
HAQ 2247+0146	Unknown	< 0.39	
HAQ 2252+0434	QSO	0.35	0.84	5.42 ± 0.08	
HAQ 2253+1141	QSO	2.40	0.17	< 0.30	
HAQ 2254+0638	M-dwarf	0.00	0.00	< 0.39	
HAQ 2300+0914	QSO	1.99	0.29	64.79 ± 0.13	Grism 6
HAQ 2301+0832	QSO	1.10	0.03	< 0.31	
HAQ 2303+0238	QSO	1.10	0.22	< 0.37	Grism 6
HAQ 2303+0630	QSO	0.99	0.36	< 0.38	
HAQ 2305+0117	QSO	2.67	0.13	< 0.40	
HAQ 2310+1117	QSO	0.83	0.92	< 0.65	
HAQ 2311+1444	QSO_HIZ	3.31	0.00	< 0.65	(SDSS legacy: $z=3.31$)
HAQ 2313+0955	QSO	1.06	0.55	< 0.65	
HAQ 2318+0255	QSO	3.50	0.00	< 0.37	
HAQ 2326+0642	QSO	1.25	0.37	< 0.39	
HAQ 2326+1423	QSO	2.54	0.17	< 0.39	
HAQ 2330+1009	QSO	3.11	0.19	18.39 ± 0.17	
HAQ 2333+0113	QSO	3.25	0.05	< 0.44	(BOSS: $z=3.28$)
HAQ 2333+0619	QSO	2.72	0.13	< 0.53	
HAQ 2335+1407	QSO	0.97	0.54	< 0.53	
HAQ 2337+1343	QSO	3.57	0.00	< 0.53	
HAQ 2339+1232	QSO	1.24	0.19	< 0.44	
HAQ 2340+0121	QSO	2.15	0.15	< 0.44	
HAQ 2343+0615	QSO	2.16	$0.29^{(a)}$	< 0.32	
HAQ 2348+0716	QSO	0.88	0.22	< 0.36	
HAQ 2351+1429	QSO	2.96	0.23	< 0.40	
HAQ 2352+0105	QSO_HIZ	2.14	0.06	< 0.40	(BOSS: $z=2.99$)
HAQ 2358+0339	QSO	2.09	0.06	< 0.36	
HAQ 2358+0359	QSO	2.89	0.20	< 0.35	
HAQ 2358+0520	QSO	3.47	0.00	< 0.37	
HAQ 2358+1436	QSO	1.05	0.65	< 0.26	

^(a) Marks systems with intervening dust. We here give the estimated $A(V)_{\text{abs}}$ at the absorber redshift assuming the LMC extinction curve.

Note. — In cases where SDSS legacy had flagged the object as QSO for follow-up this is indicated by 'QSO_HIZ' or 'QSO_CAP' as object 'Type'. In the 'Notes' column, we list the targets with spectra available in BOSS or SDSS legacy along with their inferred redshift. Other remarks such as complementary observations with different grisms are also listed here.

4.1.2. Robustness and precision of the likelihood ratio test

When determining whether a given QSO spectrum was better fitted by the general model than the null model, we assigned a probability of observing the given increase in likelihood assuming that the null model is true. We rejected the null model when this probability was below 5σ . Hence, we might have rejected the null model in cases where this was indeed the true model, and vice versa. In order to quantify how robust our method is, we therefore generate a set of model QSOs with varying amounts of both intrinsic and intervening dust. We then quantify how many absorption systems are recovered using the likelihood ratio test at different signal-to-noise ratios, and how well the input parameters are estimated by the fit. Each QSO model is described by four parameters: the QSO redshift (z_{QSO}), the extinction at the QSO redshift ($A(V)_{\text{QSO}}$), the absorber redshift (z_{abs}), and the extinction at the absorber redshift ($A(V)_{\text{abs}}$). We assume that the dust in the QSO is of SMC type in all cases and generate two sets of models with the dust in the absorber being, respectively, of SMC or LMC type. For each model, we then generate synthetic datasets mimicking the SDSS and UKIDSS photometric bands and the spectral coverage of the NOT observations. We generate 500 models of synthetic datasets for each of the absorber extinction curves (LMC or SMC) and for both high and low signal-to-noise ratios: in total 2000 models. We use the same fitting method as described in Sect. 4.1 to fit both the null model and the general model. Hereafter we apply the same criteria for rejecting the null model as were used in the analysis of our data. That way we quantify how well we were able to identify intervening systems and with what precision the parameters are recovered. For models with LMC extinction in the absorber, we recover 39.8% of the intervening systems down to $A(V)_{\text{abs}} > 0.2$ with high signal-to-noise ratio. While we at low SNR only recover 15.0% and only with $A(V)_{\text{abs}} > 0.4$. For models with SMC type extinction, we recover 18.2% of the absorbers down to $A(V)_{\text{abs}} \gtrsim 0.5$ in the high SNR data and 0.0% in the low SNR data. The precision on the best-fit parameters for the recovered intervening systems are given in Table 4 for each of the extinction curves (LMC or SMC) and for both high and low SNR. Here we show the 16th, 50th, and 84th percentile of the residuals for the three fit parameters. In Appendix B, we present the details of the recovered intervening systems along with details about the initial parameter distributions and noise models.

In order to estimate the robustness of the likelihood ratio test, we also perform a sanity check of the null hypothesis. For this we generate 2×500 spectra with dust only at the QSO redshift at high and low SNR and fit these with both the null model and the general model. In *all* cases, we reject the general model; in other words the preferred model is the model with dust only in the QSO itself. The agreement between input and best-fit parameter allows us to quantify the precision in the $A(V)$ estimates using this method of fitting templates to the data. We observe no bias in the estimated parameters and find a statistical uncertainty of ± 0.01 on the $A(V)$ estimates for high SNR, while we get ± 0.02 at low SNR. These are only statistical uncertainties; the actual error on a single measurement in *real* data may be larger due to the template not being a perfect description for every QSO.

Table 3. Dust in Intervening Absorbers

Target	z_{QSO}	z_{abs}	$A(V)_{\text{abs}}$	$A(V)_{\text{QSO}}$
HAQ0000+0557	3.31	$2.03^{+0.03}_{-0.03}$	$0.32^{+0.03}_{-0.03}$	$0.04^{+0.01}_{-0.01}$
HAQ0011+0122	1.11	$0.66^{+0.02}_{-0.02}$	$0.39^{+0.04}_{-0.05}$	$0.06^{+0.02}_{-0.02}$
HAQ0031+1328	1.02	$0.79^{+0.01}_{-0.01}$	$0.35^{+0.02}_{-0.02}$	$0.08^{+0.01}_{-0.01}$
HAQ0051+1542	1.90	$1.24^{+0.03}_{-0.03}$	$0.39^{+0.04}_{-0.03}$	$-0.15^{+0.02}_{-0.03}$
HAQ0339+0420	1.80	$1.10^{+0.06}_{-0.07}$	$0.44^{+0.07}_{-0.06}$	$0.01^{+0.03}_{-0.04}$
HAQ1248+2951	3.55	$2.36^{+0.10}_{-0.09}$	$0.20^{+0.02}_{-0.02}$	$-0.03^{+0.01}_{-0.01}$
HAQ1509+1214	2.80	$1.71^{+0.06}_{-0.04}$	$0.45^{+0.13}_{-0.12}$	$-0.15^{+0.05}_{-0.06}$
HAQ2203–0052	1.24	$0.65^{+0.04}_{-0.03}$	$0.73^{+0.07}_{-0.07}$	$-0.11^{+0.02}_{-0.03}$
HAQ2343+0615	2.16	$1.48^{+0.03}_{-0.03}$	$0.29^{+0.04}_{-0.04}$	$-0.05^{+0.03}_{-0.03}$

Note. — The estimates of $A(V)_{\text{abs}}$ are calculated assuming the LMC extinction curve by Gordon et al. (2003).

Table 4. Precision of recovered parameters from the likelihood ratio test

	High SNR			Low SNR		
	$\Delta A(V)_{\text{QSO}}$	$\Delta A(V)_{\text{abs}}$	Δz_{abs}	$\Delta A(V)_{\text{QSO}}$	$\Delta A(V)_{\text{abs}}$	Δz_{abs}
LMC	$0.00^{+0.04}_{-0.04}$	$0.01^{+0.08}_{-0.09}$	$0.00^{+0.05}_{-0.03}$	$-0.02^{+0.07}_{-0.07}$	$0.03^{+0.14}_{-0.10}$	$0.00^{+0.06}_{-0.05}$
SMC	$-0.08^{+0.12}_{-0.16}$	$0.09^{+0.24}_{-0.15}$	$0.04^{+0.17}_{-0.18}$

Note. — For each input extinction law, we show the residuals (input – output) of the various model parameters.

4.1.3. Intervening Absorption Systems

Next step is to go through all the spectra manually to look for intervening absorption systems such as DLAs or Mg II systems that would provide a host for dust at lower redshift. Due to the limited signal-to-noise ratio and low resolution we are not able to detect weak absorption systems. Also the limited wavelength coverage means that we might miss absorption systems if the Ly α or Mg II lines fall outside the spectral range for the given absorption system. We identify 27 QSOs with clearly visible absorption systems and three tentative detections (due to low signal-to-noise ratio). The systems are mainly identified by the characteristic Mg II $\lambda\lambda$ 2796, 2803 doublet, one target is identified by the Ca II $\lambda\lambda$ 3934, 3969, and eight systems are identified by Ly α , C IV, or both. The identifications are secured by detections of other absorption lines (such as Fe II lines) at the same redshift. All absorption systems are listed in Table 5. Out of the nine QSOs that have preferred solutions with intervening dust in the model comparison, two have Mg II systems at redshifts close to the best-fit absorption redshift, one target with inconsistent redshifts between the absorption system and the best-fit, and one target (HAQ2343+0615) has slight indications of a Mg II absorption system at the best-fit absorber redshift $z_{\text{abs}} = 1.49$. However, the quality of the data does not allow a firm detection.

The target, HAQ0000+0557, shows a very strong Mg II ($\text{EW}_{\text{rest}}(2796) = 4.5\text{\AA}$) absorber at $z_{\text{Mg II}} = 2.048$. This QSO is one of the QSOs for which the general model with dust in an intervening absorber was preferred, see Sect. 4.1.1. The preferred redshift for the absorber from the fitting was $z_{\text{abs}} = 2.03 \pm 0.03$ in agreement with the Mg II system. This strongly suggests that the dust reddening (with $A(V)_{\text{abs}} = 0.32$) be caused by this Mg II system. Although the spectrum is well fitted by the intervening dust model, the IR photometry is matched better by the model with only QSO dust, see top panel of Fig. 3. Further analysis of the extinction curve is needed in order to fit all the data. However, for this we would need a longer spectroscopic wavelength range observed simultaneously to rule out offsets in the photometry due to the intrinsic QSO variations.

The spectrum of HAQ0339+0420 has a Mg II absorption system at a redshift of $z_{\text{Mg II}} = 1.21$ coinciding with the preferred redshift for an intervening system from the fit at $z_{\text{abs}} = 1.10$ with $A(V)_{\text{abs}} = 0.44$. Although the best-fit redshift is lower than the redshift for the Mg II absorber, the two are consistent when considering the 3σ confidence interval for the absorber redshift $0.92 < z_{\text{abs}} < 1.24$.

The spectrum of HAQ0015+0736 shows a strong Mg II system at $z_{\text{Mg II}} = 2.47$ with a weak corresponding Ly α line. The strong absorption seen at $\lambda_{\text{obs}} \sim 4100\text{\AA}$ is caused by the Lyman limit from a sub-DLA at $z_{\text{sDLA}} = 3.49$. The best-fit template for the QSO is consistent with no reddening.

The QSO, HAQ1115+0333, was observed with grisms #6 and #7 to provide higher resolution spectroscopy of the absorber which was identified in the spectrum taken with grism #4. The QSO shows a strong Mg II absorber at $z = 1.18$ and a weaker (Lyman α , C IV) system at $z = 2.57$. However, the spectrum of this system is consistent with the dust being at the QSO redshift $z_{\text{QSO}} = 3.10$. The rest of the identified absorption systems in Table 5 are all either consistent with no dust

or with the dust residing in the QSO system only. However, one target (HAQ 2225+0527) is the exception to the rule. This system has a Damped Ly α absorption system at redshift $z_{\text{DLA}} = 2.131$. The extinction towards the QSO is quite high ($A(V) = 0.29$), and is consistent with the dust extinction being caused by SMC type dust in the DLA when taking into account the added constraint on z_{abs} . The reason why this system was not identified in our statistical analysis is due to the fact that SMC type dust is extremely difficult to identify with this approach, since the featureless extinction curve does not provide any redshift dependent features. Hence, the degeneracy between the various fit-parameters is very large. In Sect. 4.1.2, we discussed the limitations of the statistical approach and we found that for SMC type dust only absorption systems with $A(V)_{\text{abs}} \gtrsim 0.5$ are recovered. Given the value of $A(V)=0.29$ for HAQ2225+0527 we therefore do not expect to detect the intervening reddening with this particular modelling approach.

4.1.4. Spectral Energy Distributions

We investigate the average behaviour of the QSOs in our sample by stacking their rest-frame, dust-corrected energy distributions. We correct for dust assuming the best-fit reddening obtained as described above. Hereafter we linearly interpolated all the rest-frame SEDs onto a common wavelength grid. We then normalize each SED at rest-frame wavelength 5100 Å. The average SED is computed using the median as well as the 50 % and 90 % confidence intervals. The confidence intervals only take into account the variance in the sample because this, along with the interpolation, is the dominant source of uncertainty. For reference, the typical uncertainty on the photometric measurements is of the order of 5 %. In Fig. 4, we show the median SED and its confidence intervals. We show the continuum model from Richards et al. (2006) for comparison. In the top panel of the figure, we show the number of individual SEDs that contribute to a given wavelength bin.

In the blue part of the SED, for $\lambda < 1500$ Å, we observe the largest discrepancy between our data and the template. This is, however, expected due to the low number of sources contributing to the stack in this range and due to the fact that we have not corrected for BAL QSOs in our sample, which significantly redden the overall SED blue-wards of C IV. Apart from this discrepancy at short wavelengths, the sample is very homogenous for wavelengths less than rest-frame 1 μm . At larger wavelengths the sample exhibits a higher degree of variance. We therefore study the properties of the deviant SEDs at rest-frame 2 μm , since at this wavelength the number of objects contributing to the stack is still high ($> 80\%$). Above 3 μm the large variance is dominated by the fact that only a small number of objects contribute to the stack. We classify outliers as SEDs whose flux in the rest-frame 2 μm data point differs by more than 5σ from the template at the given wavelength.

In total, we find 27 QSOs that differ more than 5σ from the template at rest-frame 2 μm , 11 of which have an apparent excess compared to the template, and 16 have a deficit compared to the template. We included one additional target (HAQ1639+3157) that was not selected by this criterion because the large error on the WISE band 1 in this case falsely enhanced the uncertainty in the interpolated flux at rest-frame 2 μm . The QSOs with rest-frame infrared excess are shown in

Table 5. Intervening absorption systems.

Target	z_{QSO}	$z_{\text{spec}}^{(a)}$	$z_{\text{abs}}^{(b)}$	$A(V)_{\text{abs}}^{(b)}$	$A(V)_{\text{QSO}}$	Notes
HAQ0000+0557	3.31	2.05	2.03 ± 0.03	0.32 ± 0.03	0.04 ± 0.01	strong Mg II absorber
HAQ0008+0835	1.19	0.85	0.00	Mg II absorber
HAQ0008+0846	1.23	1.07	0.04	Mg II absorber
HAQ0015+0736	3.63	2.47	−0.05	strong Mg II absorber with associated Ly α
HAQ0015+1129	0.87	0.81	0.78	Mg II absorber
HAQ0024+1037	1.22	0.29	0.27	Ca II absorber
HAQ0044+0817	3.35	2.90	0.00	Damped Ly- α absorber
HAQ0053+0216	0.99	0.90:	0.71	Mg II absorber, low SNR
HAQ0059+1238	3.50	3.21	0.00	Ly α and C IV absorber
HAQ0143+1509	3.76	1.24	0.00	Mg II absorber
HAQ0211+1214	2.11	1.02	0.05	Mg II absorber
HAQ0337+0539	3.28	1.20	0.03	Mg II absorber
HAQ0339+0420	1.80	1.21	1.10 ± 0.07	0.44 ± 0.07	0.01 ± 0.03	Mg II absorber
HAQ0340+0408	1.62	1.03:	0.13	Mg II absorber, low SNR
HAQ0355−0053	2.15	1.24	0.00	Mg II absorber
HAQ1115+0333	3.10	1.18	0.15	Mg II absorber
HAQ1115+0333	3.10	2.57	0.15	Weak Ly α and C IV absorber
HAQ1248+2951	3.55	1.56	2.36 ± 0.10	0.20 ± 0.02	-0.03 ± 0.01	Mg II absorber
HAQ1327+3206	2.48	0.63	0.01	Mg II absorber
HAQ1355+3407	3.16	1.08	0.00	Mg II absorber
HAQ1534+0013	3.44	2.86	0.00	Damped Ly α absorber
HAQ1633+2851	1.14	0.71:	0.52	Mg II absorber, low SNR
HAQ2159+0212	1.26	1.04	0.10	Mg II absorber
HAQ2222+0604	2.45	1.29	0.25	Mg II absorber
HAQ2225+0527	2.32	2.13	0.29	Damped Ly α absorber
HAQ2231+0509	1.76	1.21	0.35	Mg II absorber
HAQ2241+0818	2.43	2.32	0.04	Damped Ly α absorber
HAQ2244+0335	3.37	2.89	0.00	Damped Ly α absorber
HAQ2303+0238	2.22	1.47	0.11	Mg II absorber
HAQ2305+0117	2.67	1.49	0.13	Mg II absorber
HAQ2305+0117	2.67	2.67	0.13	Damped Ly α absorber at QSO redshift
HAQ2311+1444	3.31	1.67	0.00	Mg II absorber

^(a) z_{spec} here denotes the spectroscopic redshift of the absorption system. Redshifts marked with : denote tentative detections due to low SNR.

^(b)Redshift and extinction values are only given in cases where the absorber model was preferred in the likelihood ratio test described in Sect. 4.1.1. The values reported here assume LMC type dust at the absorber redshift from the fit.

Fig. 5 and 6. We construct a simple model in which the excess emission is caused by re-emission from hot dust. We approximate the emission by a black-body emission with a single temperature, T_{dust} . By adding this component to the reddened template (here from Richards et al. 2006) and fitting the reddened template plus dust emission to the H and K bands along with the four WISE bands, we are able to get a very good agreement in most cases with dust-temperatures in the range of $800 \text{ K} < T_{\text{dust}} < 1600 \text{ K}$. The best-fit dust emission model is shown in Fig. 5 and 6 together with the best-fit template without extra dust emission.

The QSOs with rest-frame infrared deficit are summarized in Fig. 7. These QSOs (except three: HAQ0011+0122, HAQ1233+1304, and HAQ1527+0250; see Sect. 5.2) all have rest-frame infrared SEDs consistent with no or very little reddening, however, from our fits to the rest-frame UV and optical data we infer a significant amount of reddening. This seems to indicate a problem with the assumed extinction law. In order to test this, we re-fit the overall SED while changing the slope of the extinction law. We do this in terms of the parameter, $R_V \equiv A(V)/E(B - V)$, where $E(B - V) = A(B) - A(V)$. A large value of R_V thus gives rise to a flat extinction curve, whereas small values indicate steeper extinction curves; for comparison, the SMC extinction curve from Gordon et al. (2003) has $R_V = 2.74$. Only for two QSOs (HAQ1106+0300, HAQ0206+0624) did the fit converge, in this cases yielding $R_V = 0.8 \pm 0.2$ and $R_V = 0.6 \pm 0.2$. The other fits failed to converge or failed to reproduce the IR fluxes, however, this does not rule out the fact that the extinction law may differ from the assumed SMC law. Instead, this reflects that simply varying R_V is not enough to get the shape of the extinction curve to match the data. A detailed analysis of these extinction curves for a subset of our sample is currently underway (Zafar et al. 2014, in preparation).

All the individual SEDs are shown in Appendix C.

4.1.5. Radio Properties

We have matched our catalog to the VLA FIRST Survey (Becker et al. 1995) to check for radio detections in our sample. Although our selection has not been based on radio detections, we have compiled data from the VLA/FIRST survey to compare the radio properties in our sample with other studies, e.g., Glikman et al. (2012, 2013). The survey provides measurements at 1.4 GHz ($\lambda = 20 \text{ cm}$) with a typical rms level of 0.15 mJy. A search through the survey’s publicly available database⁶ reveals that 18 (out of 159) sources have radio detections at 1.4 GHz within a search radius of 10 arcsec. Thirteen targets in our sample lie outside the FIRST survey area. The radio fluxes (or 3σ upper limits for non-detections) are given in Table 2. We characterize the radio properties in terms of *radio loudness*. The term radio loudness has been defined in various ways, e.g., using the rest-frame radio luminosity or the ratio of radio-to-optical flux. We have chosen to use the ratio of radio-to-optical flux since this is independent of redshift and cosmological assumptions.

⁶<http://sundog.stsci.edu/index.html>

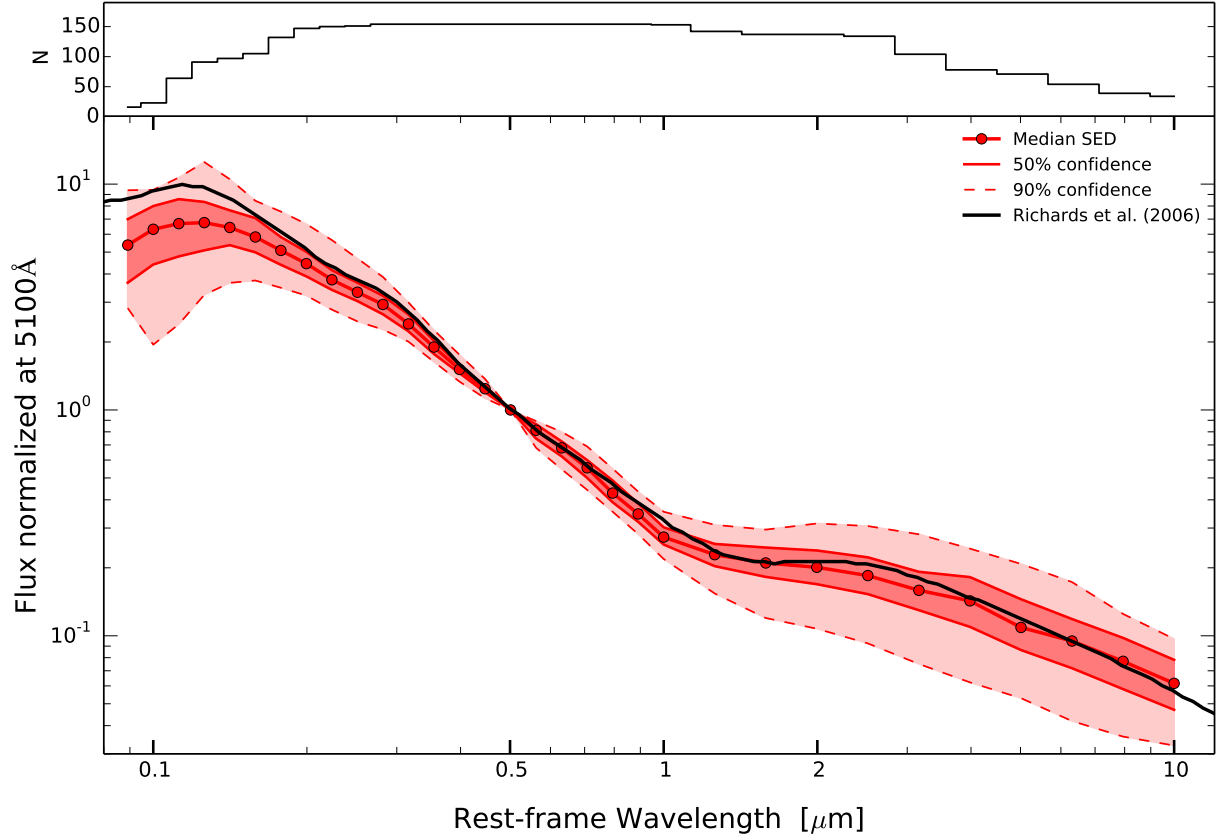


Fig. 4.— Median rest-frame stacked spectral energy distribution (SED) for all QSOs in our sample (red points). The individual SEDs have been scaled at 5100 Å before stacking. The dark and light red shaded areas show the 50% and 90% confidence intervals, respectively. The overplotted black line shows the continuum template of Richards et al. (2006). The top panel shows the number of individual SEDs that contribute to a given wavelength bin.

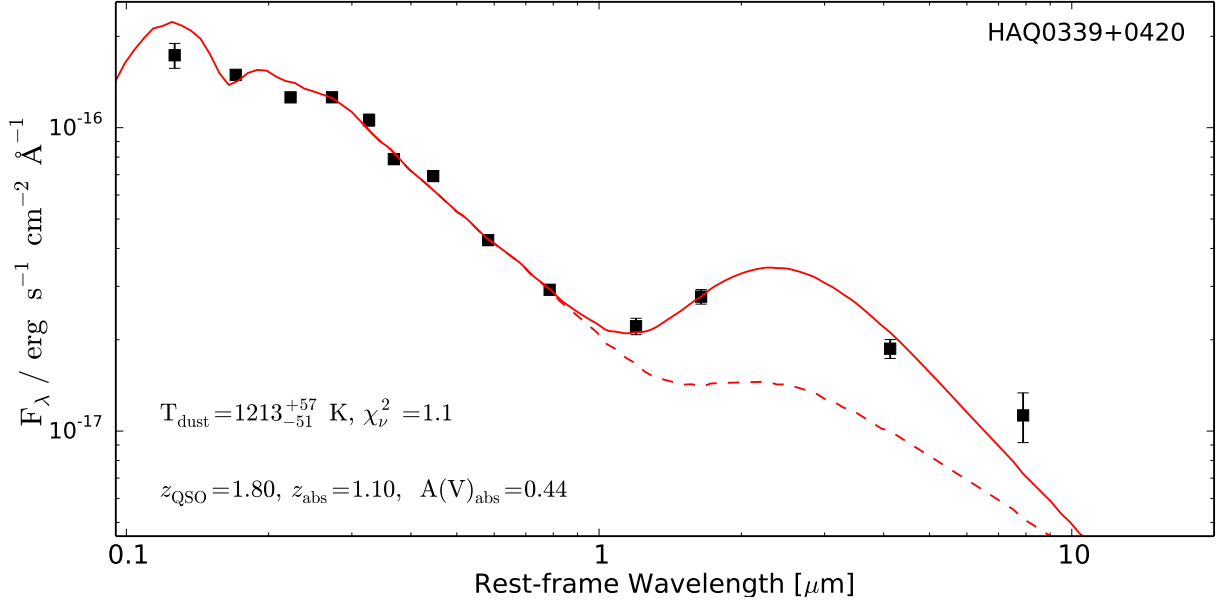


Fig. 5.— A QSO with rest-frame infrared excess at $2 \mu\text{m}$ (black points). The dashed line shows the best-fit template from fits to the spectra and SDSS and UKIDSS photometry as described in Sect. 4.1. The solid line shows the same template with an extra dust component fitted to the H , K and WISE bands. In the bottom left corner, we give the best-fit dust temperature, T_{dust} and the reduced χ^2 from the dust component fit. This particular QSO was identified as a system with intervening absorption (see Section 4.1.1), we therefore indicate the QSO redshift, the inferred absorption redshift and the best-fit extinction at the absorption redshift. We emphasize that the reddening law in the absorber’s rest-frame is assumed to be of LMC type.

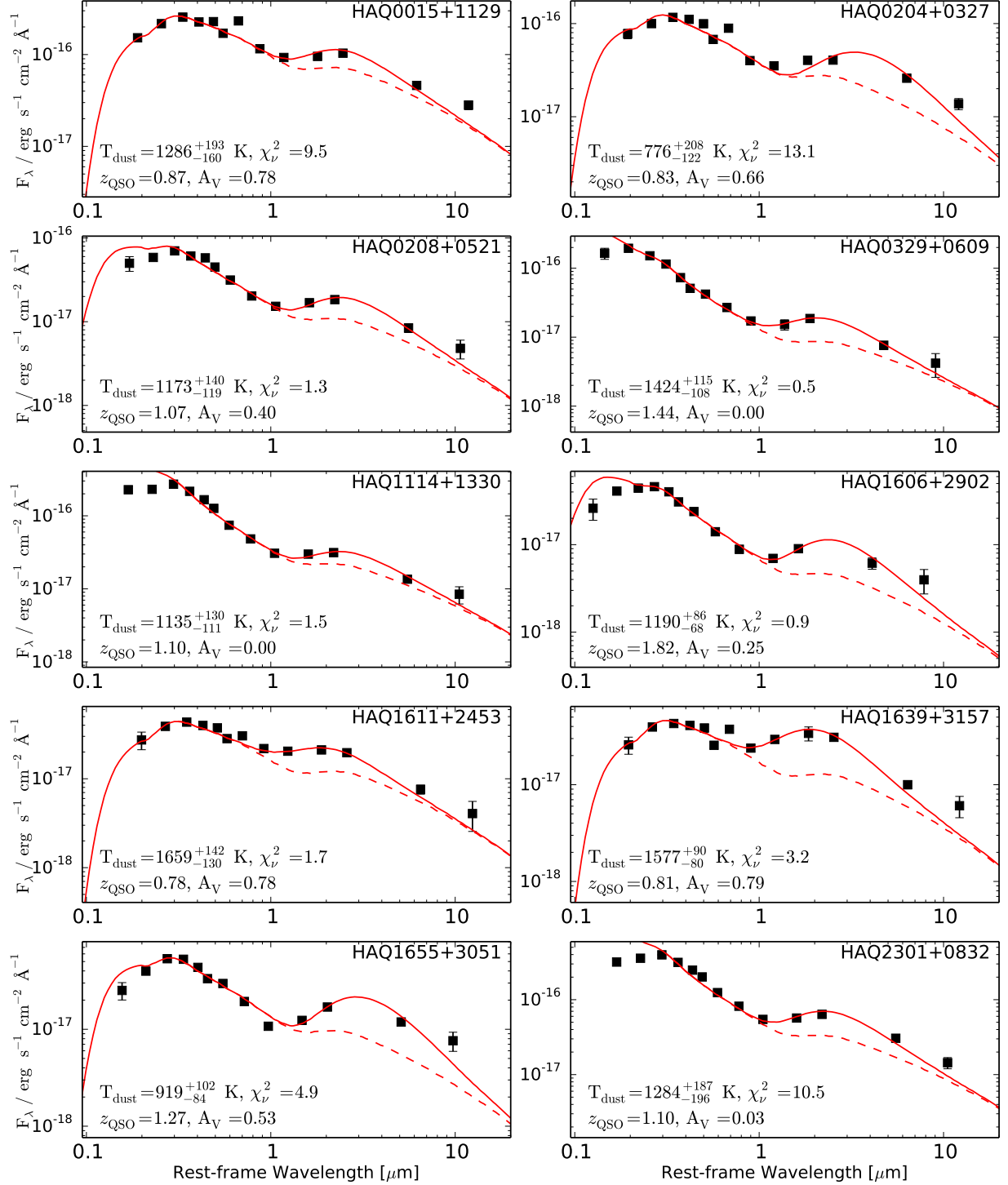


Fig. 6.— Individual QSOs with rest-frame infrared excess at $2\ \mu\text{m}$ (black points). The dashed line shows the best-fit template from fits to the spectra and SDSS and UKIDSS photometry as described in Sect. 4.1. The solid line shows the same template with an extra dust component fitted to the H , K and WISE bands. In each panel, we give the best-fit dust temperature, T_{dust} , the QSO redshift, z_{QSO} , the inferred extinction at the QSO redshift, A_V , and the reduced χ^2 from the dust component fit.

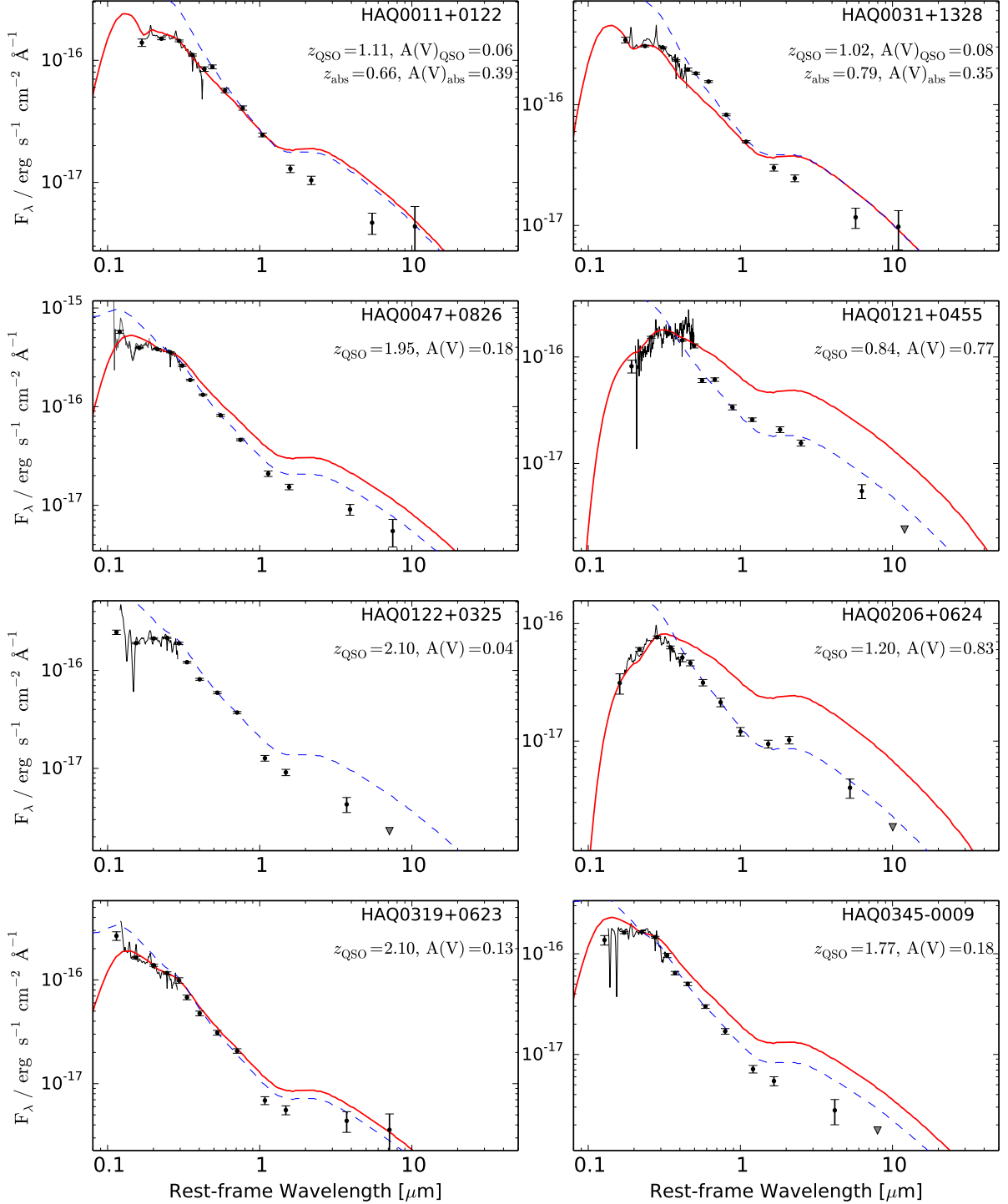


Fig. 7.— Individual QSOs with rest-frame infrared deficit at 2 μ m (black points). In each panel, the dashed, blue line shows the unreddened template from Richards et al. (2006). The red, solid line shows the same template reddened by the amount given in each panel. In two cases the reddening is very low (consistent with zero), therefore only the dashed line is shown.

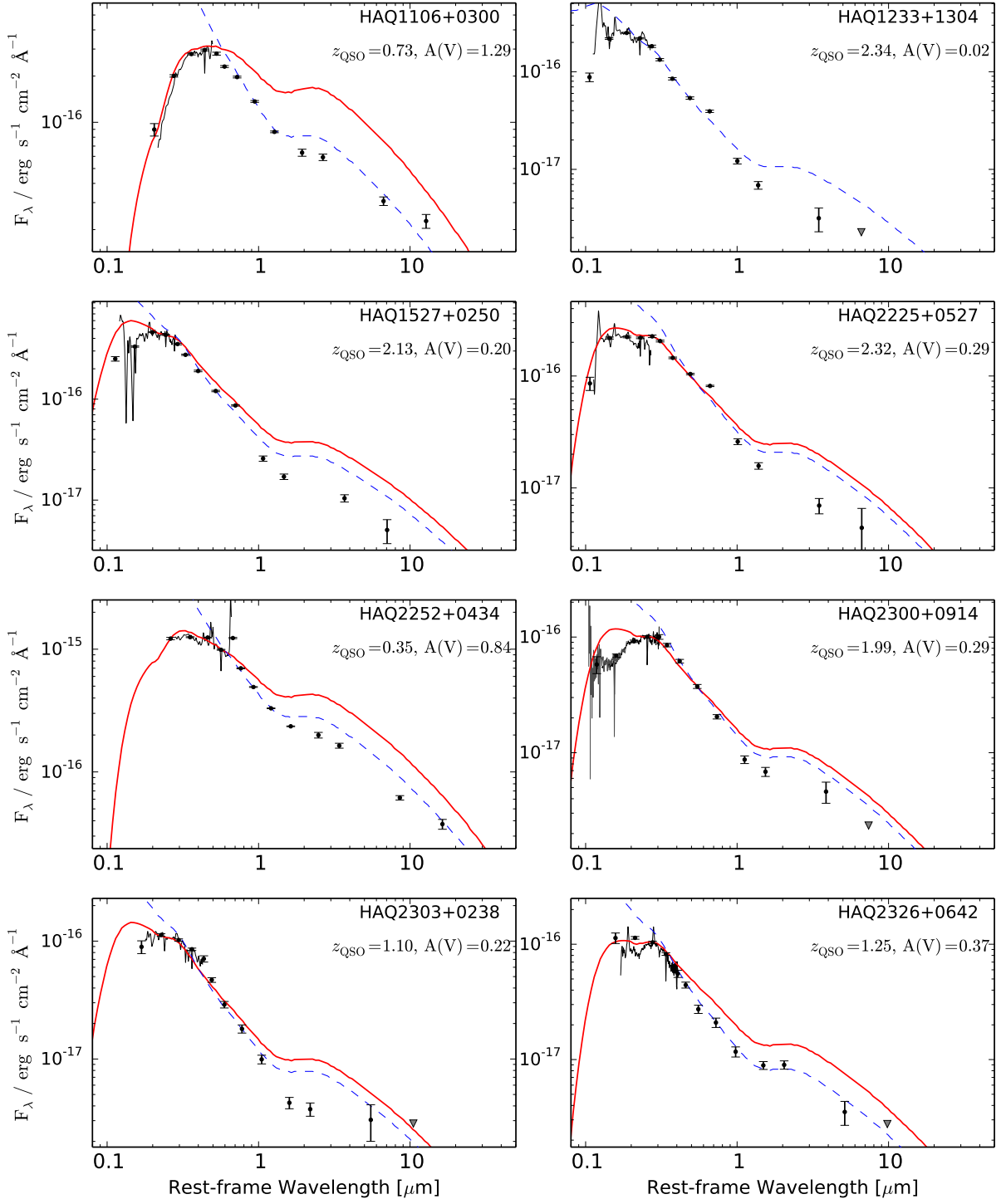


Fig. 6.— Continued.

We use the definition of the radio-to-optical ratio, R_m from Ivezić et al. (2002) to quantify the radio-loudness of QSOs. The authors define R_m as the ratio of the radio flux to the optical flux:

$$R_m = \log \left(\frac{F_{\text{radio}}}{F_{\text{optical}}} \right) = 0.4 (m - t) ,$$

where m refers to the AB magnitude in any of the SDSS bands and t is the “radio AB magnitude” at 1.4 GHz: $t = -2.5 \log \left(\frac{F_{\text{int}}}{3631 \text{ Jy}} \right)$. Following this definition, a radio-loud source will have $R_m > 1$. For our analysis we use the i band of SDSS in order to compare with the work of Ivezić et al. (2002); switching to g or r band does not change the inferred radio-loud fraction. In Fig. 8, we show the dust-corrected radio-to-optical ratio, R_{i_0} , for the detected sources in our sample using the $A(V)$ inferred from the combined fit to spectroscopy and photometry to de-redden the i -band magnitude. We also show the non-detected sources as conservative 5σ upper limits. As seen in Fig. 8, all non-detections except for four are consistent with being radio-quiet. Hence, we are able to put very firm constraints on the fraction of radio-loud QSOs. If we assume that *all* non-detections are radio-quiet (consistent at the 3σ level) we find a radio-loud fraction ranging from 9% to 12%, including the uncertainty of the dust-correction.

Ivezić et al. (2002) find a radio-loud fraction of $8 \pm 1\%$ for QSOs with $i < 18.5$. For the same i -band magnitude limit, we find a radio-loud fraction of 12–14%. A higher fraction of radio-loud QSOs would be expected when targeting red QSOs as the radio flux has been shown to correlate with optical ($g - r$) colour (White et al. 2007). We further note, that due to the colour selection of our sample, the estimate of radio-loud fraction is not representative of the overall QSO population.

4.2. Contaminants

Two objects in our sample are identified as stars (marked in Table 2): one M-dwarf and one G-dwarf. Their spectra are plotted together with stellar templates from SDSS⁷ in Appendix E. The G-dwarf template has been reddened ($A(V)=0.6$) to match the observed spectrum by assuming MW type dust from Gordon et al. (2003).

We find two objects (HAQ1607+2611 and HAQ2247+0146) that are not securely identified. The object HAQ1607+2611 is probably a QSO with very weak emission lines, whereas HAQ2247+0146 is most likely a special subclass of BAL QSOs (so-called FeLoBALs) with very strong and broad absorption on the blue side of Mg II. However, the spectra do not provide enough clues to firmly secure the identification and redshift.

⁷<http://www.sdss.org/dr5/algorithms/spectemplates>

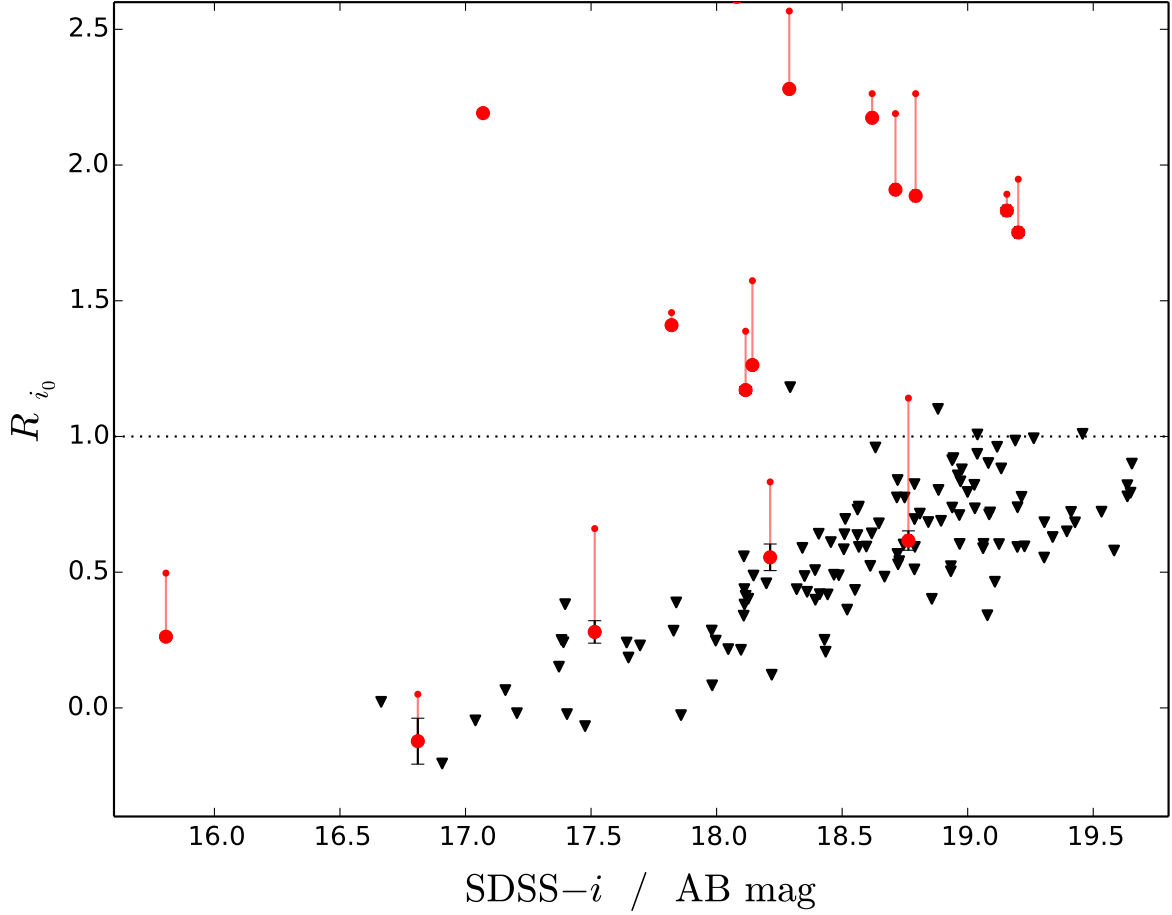


Fig. 8.— Dust corrected radio-to-optical index, R_{i_0} , as function of observed i band magnitude are shown as red circles with error bars. The small red dots connected by thin lines to each data point mark the values of R_i before correcting for dust. The dotted horizontal line marks the proposed boundary between radio loud ($R > 1$) and radio quiet ($R < 1$). Non-detections from our sample are shown as 5σ upper limits (black triangles).

5. Discussion

Our primary goal was to search for intervening absorption systems hosting metals and dust, which would go undetected in optically selected samples of QSOs (e.g., SDSS-I/II). We found 30 such absorption systems, however, with varying amounts of dust. Moreover, we found interesting dust features most likely caused by dust within the QSO system. In the following we take a closer look at the intervening systems in our sample and at the dust properties in the environment of the QSOs.

5.1. Dust in Intervening Absorbers

In order to check whether any of the QSOs showed signs of intervening absorption, we analysed all the spectra with an automated likelihood algorithm. In Sect. 4.1.1, we found nine cases where the code returned a preferred intervening dusty system. These are listed in Table 3. For all nine systems, we found that the extinction was caused by dust in the absorber only; the extinction at the QSO redshift was consistent with no reddening. All the other systems in our sample were fully consistent with either no reddening or dust at the QSO redshift, but note that our method is mainly sensitive to intervening absorbers with extinction curves displaying the 2175 Å extinction feature (see below).

Most statistical studies of absorption systems (Mg II or DLAs) find that the average reddening, though small, is consistent with SMC type extinction (York et al. 2006; Vladilo et al. 2008; Khare et al. 2012). However, indications of the 2175 Å bump, typical in Milky Way and LMC sightlines, are observed in some cases both statistically using stacking (Malhotra 1997) and in individual absorbers (Junkkarinen et al. 2004; Wang et al. 2004; Ellison et al. 2006; Srianand et al. 2008; Elíasdóttir et al. 2009; Noterdaeme et al. 2009a; Jiang et al. 2010; Zhou et al. 2010; Jian-Guo et al. 2012; Zafar et al. 2012). Interestingly, we found *no* systems with preferred SMC extinction in an intervening system from our algorithm although the overall population seems to indicate SMC type dust. This is, however, to be expected when taking into account the limitations of the method we utilized. In Sect. 4.1.2, we found that absorbers needed to cause very high extinction ($A(V) \gtrsim 0.5$) with the SMC law in order to be detected, even at high SNR. This is due to the high degeneracy between dust at the absorber redshift and intrinsic dust in the QSO because the SMC extinction curve is mostly featureless. Our simulations showed that we were much more sensitive to LMC type extinction due to the very characteristic 2175 Å bump which provided a rather unique imprint in the spectra. This allowed for a much more secure determination of the redshift of the absorber if this feature was available in the spectrum. Still, we are limited to absorbers with extinction higher than $A(V) > 0.2$ at high SNR (an average SNR per spectral pixel of 15).

Since these estimates were purely based on statistical modelling, the results could be improved if an absorption system at a corresponding redshift could be identified. This would then serve as an anchor for z_{abs} , which allows us to measure the extinction curve in the absorber with greater

precision. For the nine cases reported here, two of them had a detection of a Mg II absorption system close to the best-fit redshift and one sightline showed a tentative detection. This indicates that the dust model was indeed detecting physical features and not just artefacts in the spectra. Furthermore, one DLA was found to be a plausible host of SMC type dust causing reddening of the background QSO when restricting the dust absorber redshift. This system, which will be discussed in more detail in a future work, is the kind of system we originally looked for with this survey.

Our results suggest that previous studies of dust extinction caused by intervening absorbers might have been biased against LMC type dust. This is plausibly caused by two effects. On one hand, for absorbers causing low amounts of extinction (as is usually the case for intervening absorbers found to date) the 2175 Å feature characteristic of the LMC and MW extinction curves may be very weak. This will generally lead an observer to classify the extinction as SMC type, as the 2175 Å bump disappears in the noise (see discussion in Khare et al. 2012). On the other hand, for dust-rich absorbers causing high amounts of extinction, where a distinction between various extinction curves is more easily done, the reddening of the background QSO may cause the QSO to drop out of the optical colour selection utilized in previous samples. It has indeed been shown that such highly reddened QSOs are underrepresented in previous samples of QSOs from optical colour selection (Fynbo et al. 2013; Glikman et al. 2012, 2013). However, with the advance in near- and far-infrared photometric surveys and various new QSO classification algorithms populations of highly reddened QSOs will be identified in larger numbers (Maddox et al. 2012; Graham et al. 2014).

5.2. Dust in the QSOs

For our entire sample, we find a median attenuation of $A(V) = 0.13$, corresponding to a median $E(B - V)$ of 0.047, assuming the value of $R_V = 2.74$ from Gordon et al. (2003). The individual dust-corrected SEDs show a very homogeneous behaviour at wavelengths $\lambda < 1\mu\text{m}$. However, at larger wavelengths we see some variance. We find that the QSOs with excess IR flux can be explained well by a simple single-temperature blackbody dust component. The dust temperatures inferred in these cases lie in the range from $800 \lesssim T_{\text{dust}} \lesssim 1600$ K with typical uncertainties of 100 – 200 K. This is in good agreement with dust temperatures found in AGN environments (Sanders et al. 1989; Rodríguez-Ardila & Mazzalay 2006). In the cases of very bad fits (e.g., HAQ0204+0327), the discrepancy might be explained by adding a host galaxy component or a model with multiple dust temperatures. However, such modelling is beyond the scope of this discussion and is not possible due to the few data points currently available in this wavelength range.

As mentioned in Sect. 4, we find 16 cases where the flux at rest-frame $2\mu\text{m}$ is significantly lower than what is predicted by the template. There may be more such QSOs, but we chose a conservative cut at 5σ to limit the influence of template variance. In these cases, the mismatch seems to hint at a problem with the assumed extinction law, since the unreddened template in all but two cases provide a good fit in the rest-frame infrared and optical, while a large amount of reddening is required to fit

the rest-frame ultraviolet data. Although uncommon, similarly steep extinction curves have been observed in previous works (e.g., Larson et al. 1996; Welty & Fowler 1992; Hall et al. 2002; Fynbo et al. 2013; Jiang et al. 2013; Leighly et al. 2014, Fynbo et al. (2014), submitted to A&A). For the two targets where this is not the case (HAQ0011+0122 and HAQ1233+1304), the lack in flux may be explained by intrinsic differences in the QSO energy distribution relative to the template. A lack of dust emission compared to the template would explain the lower rest-frame IR fluxes in these cases. This was also noted by Richards et al. (2006). Internal variations in the dust emission (both deficit and excess) may be linked to physical properties in the obscuring material, such as temperature, geometry and viewing effects (inclination).

In targets where we see indications of non-SMC type dust, we need an extinction curve that is *steeper* or with different curvature than SMC in order to explain the strong UV reddening and little or no reddening in the infrared. In Sect. 4.1.4, we modelled this behaviour of the extinction law by varying the value of R_V . This analysis only converged to meaningful values (non-negative values for $A(V)$ and R_V) for two QSO, which resulted in best-fit values of $R_V = 0.8 \pm 0.2$ and $R_V = 0.6 \pm 0.2$. This indeed hints at the need for a very steep extinction curve, but this should only be taken as a preliminary analysis. In Paper I, we reported similar indications of extinction curve mismatches. Furthermore, many of these targets exhibit extremely weak emission lines, indicating that the central region, which is emitting these lines, may be somewhat obscured. These QSOs are similar to the peculiar, red QSOs discussed by Hall et al. (2002), Meusinger et al. (2012) and Jiang et al. (2013). The QSOs found by Hall et al. (2002) show similar characteristics, i.e., missing strong emission lines and a continuum mismatch at wavelengths shorter than $\lambda < 3000 \text{ \AA}$. Many plausible explanations for such a continuum shape are discussed by these authors, however, they conclude that a steeper extinction curve (steeper than SMC or with different shape, e.g., a break) is the most likely explanation given the apparent lack of BAL features. Similar conclusions are reached by Meusinger et al. (2012).

In contrast to the QSOs in the studies of Meusinger et al. and Hall et al., four of the peculiar QSOs in this work show BAL features, two of which (HAQ1527+0250 and HAQ1233+1304) show very little apparent reddening, consistent with $A(V)=0$. The two remaining BAL QSOs (HAQ0047+0826 and HAQ0345-0009), which show signs of non-SMC type dust, both have very weak emission lines and their SEDs at $\lambda > 3000 \text{ \AA}$ are well represented by the unreddened QSO template. Further work on larger samples over a larger wavelength range is needed to shed light on the nature of these peculiar targets and to investigate the actual shape of the extinction curve needed to explain the SEDs of these QSOs. Similar steep extinction curves have been observed towards the Milky Way centre (Nishiyama et al. 2008, 2009; Sumi 2004). It is thus not clear whether the detections towards these reddened QSOs are caused by the central engine in the QSOs or simply by the fact that we observe the central parts of the host galaxy. Leighly et al. (2014) argue that by modelling the dust around the QSO with a spherical geometry and dust grain properties similar to those of the LMC or the Milky Way they can reproduce the steep extinction curve in the rest-frame UV observed in Mrk 231. In this case the dust in the central region is provided by a central star-

burst. The scattering and absorption properties of the dust in a spherical distribution then gives rise to multiple scatterings, which causes the UV photons to suffer from higher extinction than the redder wavelengths. In contrast to the results of Leighly et al., Jiang et al. (2013) use a different grain size distribution to reproduce a similarly steep extinction curve towards a high-redshift QSO. In the work of Jiang et al., the steep extinction curve is caused by a lack of larger grains, i.e., their grain size distribution is truncated at a maximum size of 70 nm. The authors invoke dust destruction in the QSO environment as a plausible mechanism, or differences in dust production and growth in QSO outflows (as argued by Elvis, Marengo, & Karovska 2002). This lack of large grains causes extinction in the UV to be relatively higher than in the optical and near-infrared. The question about the origin of the steep extinction curve is thus still open for debate. Furthermore, as is noted by Leighly et al., it is curious why this anomalous type of extinction is only observed towards a few reddened QSOs and not seen in the overall population of reddened QSOs.

6. Conclusions

In this paper, we present a clean selection method that only relies on optical and near-infrared photometry down to a flux limit of $J_{AB} < 19$, i.e., we do not require detections from radio or X-ray surveys. The method is a modification of the criteria applied in Paper I rejecting the small contamination of cool stars and evolved galaxies found in Paper I. The refined method allows us to effectively select reddened QSOs regardless of their X-ray and radio properties over a large area of the sky. In our sample of 159 objects only two turn out not to be QSOs and two remain unidentified. Our primary goal with this selection was not to compile a complete sample of red QSOs, instead we designed the criteria to give a high purity to investigate any hidden population of absorption systems towards heavily reddened QSOs. We used a statistical algorithm to identify whether the SEDs were more well-represented by dust in the QSO or in an intervening system. This way we identified 9 QSOs where dust in an intervening system was preferred. All of these were identified as having LMC type dust showing signs of the 2175 Å feature. Two (tentatively three) of these systems have Mg II absorption at a corresponding redshift to the best-fit redshift indicating that the statistical modelling was capable of correctly identifying dust in absorption systems. Moreover, we discovered a DLA towards a highly reddened QSO. Although this system was not selected in our likelihood ratio test, the data are consistent with the dust reddening being caused by SMC type dust in the DLA. This system will be studied in more detail in a forthcoming paper.

Complementary to our primary search for dusty intervening systems, our selection serendipitously discovered QSOs with a wide range of dust properties. More work on expanding the sample and quantifying the physical dust properties towards these obscured QSOs is currently underway. A complete list of all the candidate QSOs in our survey is given in Table 7 in Appendix F. <http://dark-cosmology.dk/~krogager/redQSOs/targets.html>

The authors thank the many students who dedicated their time to observing red QSOs during

the summer schools at the Nordic Optical Telescope in the years 2012 and 2013. JK acknowledges support from a studentship at European Southern Observatory in Chile. JPUF acknowledges support from the ERC-StG grant EGGS-278202. The Dark cosmology centre is funded by the DNRF. Funding for the SDSS and SDSS-II has been provided by the Alfred P. Sloan Foundation, the Participating Institutions, the National Science Foundation, the U.S. Department of Energy, the National Aeronautics and Space Administration, the Japanese Monbukagakusho, the Max Planck Society, and the Higher Education Funding Council for England. The SDSS Web Site is <http://www.sdss.org/>. The SDSS is managed by the Astrophysical Research Consortium for the Participating Institutions. The Participating Institutions are the American Museum of Natural History, Astrophysical Institute Potsdam, University of Basel, University of Cambridge, Case Western Reserve University, University of Chicago, Drexel University, Fermilab, the Institute for Advanced Study, the Japan Participation Group, Johns Hopkins University, the Joint Institute for Nuclear Astrophysics, the Kavli Institute for Particle Astrophysics and Cosmology, the Korean Scientist Group, the Chinese Academy of Sciences (LAMOST), Los Alamos National Laboratory, the Max-Planck-Institute for Astronomy (MPIA), the Max-Planck-Institute for Astrophysics (MPA), New Mexico State University, Ohio State University, University of Pittsburgh, University of Portsmouth, Princeton University, the United States Naval Observatory, and the University of Washington. We acknowledge the use of UKIDSS data. The United Kingdom Infrared Telescope is operated by the Joint Astronomy Centre on behalf of the Science and Technology Facilities Council of the U.K. This publication makes use of data products from the Wide-field Infrared Survey Explorer, which is a joint project of the University of California, Los Angeles, and the Jet Propulsion Laboratory/California Institute of Technology, funded by the National Aeronautics and Space Administration.

REFERENCES

- Banerji, M., McMahon, R. G., Hewett, P. C., Alaghband-Zadeh, S., Gonzalez-Solares, E., & Venemans, B. P. 2012, ArXiv e-prints
- Becker, R. H., White, R. L., & Helfand, D. J. 1995, *ApJ*, 450, 559
- Benn, C. R., Vigotti, M., Carballo, R., Gonzalez-Serrano, J. I., & Sánchez, S. F. 1998, *MNRAS*, 295, 451
- Croom, S. M., Smith, R. J., Boyle, B. J., Shanks, T., Miller, L., Outram, P. J., & Loaring, N. S. 2004, *MNRAS*, 349, 1397
- Dawson, K. S., et al. 2013, *AJ*, 145, 10
- Elíasdóttir, Á., et al. 2009, *ApJ*, 697, 1725
- Ellison, S. L., et al. 2006, *MNRAS*, 372, L38
- Elvis, M., Marengo, M., & Karovska, M. 2002, *ApJ*, 567, L107

- Fitzpatrick, E. L., & Massa, D. 2005, *AJ*, 130, 1127
- Foreman-Mackey, D., Hogg, D. W., Lang, D., & Goodman, J. 2013, *PASP*, 125, 306
- Fynbo, J. P. U., Krogager, J.-K., Venemans, B., Noterdaeme, P., Vestergaard, M., Møller, P., Ledoux, C., & Geier, S. 2013, *ApJS*, 204, 6
- Fynbo, J. P. U., et al. 2011, *MNRAS*, 413, 2481
- Glikman, E., Helfand, D. J., & White, R. L. 2006, *ApJ*, 640, 579
- Glikman, E., Helfand, D. J., White, R. L., Becker, R. H., Gregg, M. D., & Lacy, M. 2007, *ApJ*, 667, 673
- Glikman, E., et al. 2012, *ApJ*, 757, 51
- . 2013, *ApJ*, 778, 127
- Gordon, K. D., Clayton, G. C., Misselt, K. A., Landolt, A. U., & Wolff, M. J. 2003, *ApJ*, 594, 279
- Graham, M. J., Djorgovski, S. G., Drake, A. J., Mahabal, A. A., Chang, M., Stern, D., Donalek, C., & Glikman, E. 2014, *ArXiv:1401.1785*
- Gregg, M. D., Lacy, M., White, R. L., Glikman, E., Helfand, D., Becker, R. H., & Brotherton, M. S. 2002, *ApJ*, 564, 133
- Hall, P. B., et al. 2002, in *Astronomical Society of the Pacific Conference Series*, Vol. 255, *Mass Outflow in Active Galactic Nuclei: New Perspectives*, ed. D. M. Crenshaw, S. B. Kraemer, & I. M. George, 161
- Hopkins, P. F., et al. 2004, *AJ*, 128, 1112
- Ivezić, Ž., et al. 2002, *AJ*, 124, 2364
- Jian-Guo, W., et al. 2012, *ArXiv e-prints*
- Jiang, P., Ge, J., Prochaska, J. X., Wang, J., Zhou, H., & Wang, T. 2010, *ApJ*, 724, 1325
- Jiang, P., et al. 2013, *AJ*, 145, 157
- Junkkarinen, V. T., Cohen, R. D., Beaver, E. A., Burbidge, E. M., Lyons, R. W., & Madejski, G. 2004, *ApJ*, 614, 658
- Kaplan, K. F., Prochaska, J. X., Herbert-Fort, S., Ellison, S. L., & Dessauges-Zavadsky, M. 2010, *PASP*, 122, 619
- Khare, P., vanden Berk, D., York, D. G., Lundgren, B., & Kulkarni, V. P. 2012, *MNRAS*, 419, 1028

- Lacy, M., Petric, A. O., Sajina, A., Canalizo, G., Storrie-Lombardi, L. J., Armus, L., Fadda, D., & Marleau, F. R. 2007, *AJ*, 133, 186
- Larson, K. A., Whittet, D. C. B., & Hough, J. H. 1996, *ApJ*, 472, 755
- Leighly, K. M., Terndrup, D. M., Baron, E., Lucy, A. B., Dietrich, M., & Gallagher, S. C. 2014, *ApJ*, 788, 123
- Maddox, N., Hewett, P. C., Péroux, C., Nestor, D. B., & Wisotzki, L. 2012, *MNRAS*, 424, 2876
- Maddox, N., Hewett, P. C., Warren, S. J., & Croom, S. M. 2008, *MNRAS*, 386, 1605
- Matthews, T. A., & Sandage, A. R. 1963, *ApJ*, 138, 30
- Meusinger, H., Schalldach, P., Scholz, R.-D., in der Au, A., Newholm, M., de Hoon, A., & Kaminsky, B. 2012, *A&A*, 541, A77
- Nishiyama, S., Nagata, T., Tamura, M., Kandori, R., Hatano, H., Sato, S., & Sugitani, K. 2008, *ApJ*, 680, 1174
- Nishiyama, S., Tamura, M., Hatano, H., Kato, D., Tanabé, T., Sugitani, K., & Nagata, T. 2009, *ApJ*, 696, 1407
- Noterdaeme, P., et al. 2012, *A&A*, 540, A63
- Noterdaeme, P., Ledoux, C., Srianand, R., Petitjean, P., & Lopez, S. 2009a, *A&A*, 503, 765
- Noterdaeme, P., Petitjean, P., Ledoux, C., López, S., Srianand, R., & Vergani, S. D. 2010, *A&A*, 523, A80+
- Noterdaeme, P., Petitjean, P., Ledoux, C., & Srianand, R. 2009b, *A&A*, 505, 1087
- Peth, M. A., Ross, N. P., & Schneider, D. P. 2011, *AJ*, 141, 105
- Polletta, M. d. C., et al. 2006, *ApJ*, 642, 673
- Pontzen, A., & Pettini, M. 2009, *MNRAS*, 393, 557
- Richards, G. T., et al. 2001, *AJ*, 121, 2308
- . 2003, *AJ*, 126, 1131
- . 2006, *ApJS*, 166, 470
- Rodríguez-Ardila, A., & Mazzalay, X. 2006, *MNRAS*, 367, L57
- Sanders, D. B., Phinney, E. S., Neugebauer, G., Soifer, B. T., & Matthews, K. 1989, *ApJ*, 347, 29
- Schlegel, D. J., Finkbeiner, D. P., & Davis, M. 1998, *ApJ*, 500, 525

- Srianand, R., Gupta, N., Petitjean, P., & Saikia, D. J. 2008, MNRAS, 391, L69
- Stein, W. A., Odell, S. L., & Strittmatter, P. A. 1976, ARA&A, 14, 173
- Sumi, T. 2004, MNRAS, 349, 193
- Urrutia, T., Becker, R. H., White, R. L., Glikman, E., Lacy, M., Hodge, J., & Gregg, M. D. 2009, ApJ, 698, 1095
- van Dokkum, P. G. 2001, PASP, 113, 1420
- Vanden Berk, D. E., et al. 2001, AJ, 122, 549
- Vladilo, G., Prochaska, J. X., & Wolfe, A. M. 2008, A&A, 478, 701
- Wang, J., Hall, P. B., Ge, J., Li, A., & Schneider, D. P. 2004, ApJ, 609, 589
- Warren, S. J., Hambly, N. C., Dye, S., Almaini, O., Cross, N. J. G., & Edge, A. C. e. a. 2007, MNRAS, 375, 213
- Warren, S. J., Hewett, P. C., & Foltz, C. B. 2000, MNRAS, 312, 827
- Welty, D. E., & Fowler, J. R. 1992, ApJ, 393, 193
- White, R. L., Helfand, D. J., Becker, R. H., Glikman, E., & de Vries, W. 2007, ApJ, 654, 99
- York, D. G., et al. 2000, AJ, 120, 1579
- . 2006, MNRAS, 367, 945
- Zafar, T., et al. 2012, ApJ, 753, 82
- Zhou, H., Ge, J., Lu, H., Wang, T., Yuan, W., Jiang, P., & Shan, H. 2010, ApJ, 708, 742

A. Uncertainty Estimates

In order to estimate the confidence intervals of the best-fit parameters, we used a MCMC method. The simulations were performed using the `emcee` package for Python (Foreman-Mackey et al. 2013). We used flat priors on all parameters and ran 100 walkers for 700 iterations of which the first 100 were discarded as the "burn in" phase. In Table 6, we give the 68% and 99.7% confidence intervals of the parameter distributions.

Table 6. Dust Model Comparison

Target	z_{QSO}	Null Model		z_{abs}	$A(V)_{\text{abs}}$	$A(V)_{\text{QSO}}$	General Model		p	
		χ^2_0	$P_{\text{KS},0}$				χ^2_{G}	$P_{\text{KS},\text{G}}$		
HAQ0000+0557	3.31	0.13 ± 0.01	380.1	0.002	$2.03^{+0.03}_{-0.03}(1\sigma)^{+0.08}_{-0.08}(3\sigma)$	$0.32^{+0.03}_{-0.03}(1\sigma)^{+0.11}_{-0.09}(3\sigma)$	$0.04^{+0.01}_{-0.01}(1\sigma)^{+0.04}_{-0.04}(3\sigma)$	257.2	0.914	$2.1 \cdot 10^{-27}$
HAQ0011+0122	1.11	0.27 ± 0.01	345.6	0.135	$0.66^{+0.02}_{-0.02}(1\sigma)^{+0.05}_{-0.05}(3\sigma)$	$0.39^{+0.04}_{-0.05}(1\sigma)^{+0.14}_{-0.13}(3\sigma)$	$0.06^{+0.02}_{-0.02}(1\sigma)^{+0.07}_{-0.07}(3\sigma)$	250.0	0.347	$1.7 \cdot 10^{-21}$
HAQ0031+1328	1.02	0.28 ± 0.01	692.0	0.001	$0.79^{+0.01}_{-0.01}(1\sigma)^{+0.03}_{-0.04}(3\sigma)$	$0.35^{+0.02}_{-0.02}(1\sigma)^{+0.07}_{-0.07}(3\sigma)$	$0.08^{+0.01}_{-0.01}(1\sigma)^{+0.04}_{-0.04}(3\sigma)$	472.4	0.803	$2.1 \cdot 10^{-48}$
HAQ0051+1542	1.90	0.13 ± 0.01	362.4	0.002	$1.24^{+0.03}_{-0.03}(1\sigma)^{+0.10}_{-0.08}(3\sigma)$	$0.39^{+0.04}_{-0.03}(1\sigma)^{+0.11}_{-0.09}(3\sigma)$	$-0.15^{+0.02}_{-0.03}(1\sigma)^{+0.07}_{-0.08}(3\sigma)$	211.8	0.750	$2.0 \cdot 10^{-33}$
HAQ0339+0420	1.80	0.23 ± 0.01	167.1	0.797	$1.10^{+0.06}_{-0.07}(1\sigma)^{+0.14}_{-0.18}(3\sigma)$	$0.44^{+0.07}_{-0.06}(1\sigma)^{+0.22}_{-0.17}(3\sigma)$	$0.01^{+0.03}_{-0.04}(1\sigma)^{+0.09}_{-0.13}(3\sigma)$	112.9	0.625	$1.7 \cdot 10^{-12}$
HAQ1248+2951	3.55	0.01 ± 0.01	298.9	0.148	$2.36^{+0.10}_{-0.09}(1\sigma)^{+0.26}_{-0.21}(3\sigma)$	$0.20^{+0.02}_{-0.02}(1\sigma)^{+0.10}_{-0.06}(3\sigma)$	$-0.03^{+0.01}_{-0.01}(1\sigma)^{+0.02}_{-0.04}(3\sigma)$	184.8	0.806	$1.7 \cdot 10^{-25}$
HAQ1509+1214	2.80	0.09 ± 0.01	182.6	0.016	$1.71^{+0.06}_{-0.04}(1\sigma)^{+0.27}_{-0.11}(3\sigma)$	$0.45^{+0.13}_{-0.12}(1\sigma)^{+0.36}_{-0.28}(3\sigma)$	$-0.15^{+0.05}_{-0.06}(1\sigma)^{+0.12}_{-0.16}(3\sigma)$	127.0	0.381	$8.4 \cdot 10^{-13}$
HAQ2203-0052	1.24	0.13 ± 0.01	391.6	0.545	$0.65^{+0.04}_{-0.03}(1\sigma)^{+0.09}_{-0.08}(3\sigma)$	$0.73^{+0.07}_{-0.07}(1\sigma)^{+0.20}_{-0.22}(3\sigma)$	$-0.11^{+0.02}_{-0.03}(1\sigma)^{+0.08}_{-0.08}(3\sigma)$	297.0	0.257	$2.9 \cdot 10^{-21}$
HAQ2343+0615	2.16	0.17 ± 0.01	193.2	0.203	$1.48^{+0.03}_{-0.03}(1\sigma)^{+0.08}_{-0.11}(3\sigma)$	$0.29^{+0.04}_{-0.04}(1\sigma)^{+0.13}_{-0.12}(3\sigma)$	$-0.05^{+0.03}_{-0.03}(1\sigma)^{+0.09}_{-0.10}(3\sigma)$	144.2	0.404	$2.3 \cdot 10^{-11}$

Note. — Model parameters for the null model and the general model for the QSOs where the null model was rejected. P_{KS} refers to the p -value from the KS-test of the normalized residuals, and p refers to the chance probability of the observed improvement in χ^2 given the two extra free parameters in the general model.

B. Robustness of the Likelihood Ratio Test

In order to test the robustness of the likelihood method, we generate a set of mock QSO datasets and analyse them with our algorithm the same way as we analysed our data. Below we summarize the details of how the datasets were generated. The initial parameters were drawn randomly, following a uniform distribution, within the following limits. For the QSO redshift we use: $1 < z_{\text{QSO}} < 3.5$; for the extinction at the QSO redshift we constrain the $A(V)$ to be $A(V)_{\text{QSO}} > -0.1$. The selection of candidates in terms of $g - r$ color implies that the extinction in the QSO's rest-frame will be redshift dependent. Assuming the SMC extinction law in the QSO's rest-frame, this means that less reddening is needed at higher redshifts in order to match the $g - r$ color criterion ($0.5 < g - r < 1$). We mimic this selection effect by invoking the following limit on the modelled extinction at the QSO redshift: $A(V)_{\text{QSO}} < 1.5 - 0.37 \times z_{\text{QSO}}$. For the extinction at the absorber redshift we use: $0 < A(V)_{\text{abs}} < 1.0$; and for the absorber redshift we use: $0.1 < z_{\text{abs}} < 0.9 \times z_{\text{QSO}}$. Here the upper limit is invoked to keep the absorption redshift well-defined in the fits. This also ensures that the absorption system will be physically separated from the QSO environment.

These four randomly drawn parameters are used to generate a QSO model assuming the combined QSO template by Vanden Berk et al. (2001); Glikman et al. (2006). We use the SMC extinction curve for the reddening at the QSO redshift and we generate two sets of models: one assuming SMC type dust in the absorber and one assuming LMC type dust. The QSO model is then smoothed to match the resolution of the ALFOSC instrument at the Nordic Optical Telescope and hereafter interpolated onto a wavelength grid similar to the spectral data from the aforementioned instrument. Then we generate synthetic photometric data by calculating the flux in each of the SDSS (*ugriz*) and UKIDSS (*YJHK_s*) bands by weighting the model with the appropriate filter curve. We denote the synthetic spectral and photometric data as a *synthetic dataset*.

We then add noise to the synthetic dataset following a Gaussian noise model. We generate two sets for each assumed absorber extinction curve: one with high SNR and one with low SNR. High and low signal-to-noise ratios here refer to $\text{SNR}_{\text{spec}} = 15$, $\text{SNR}_{\text{phot}} = 20$ and $\text{SNR}_{\text{spec}} = 5$, $\text{SNR}_{\text{phot}} = 10$, respectively, where SNR_{spec} refers to the average SNR per pixel in the synthetic spectral data and SNR_{phot} refers to the SNR of each synthetic photometric band. For the spectral noise model, we further add a noise component mimicking the fringing in the red part of the CCD of the ALFOSC spectrograph. Specifically this is $\sim 20\%$ (peak-to-peak fringe level) for wavelengths greater than 8000 Å.

In the following figures, we show the results of the analysis of our synthetic datasets. In Fig. 9, we show the analysis of the models with dust added only at the QSO redshift. We plot the difference between input parameter and the recovered best-fit parameter as function of input extinction and input QSO redshift. We observe no bias and the 1σ scatter in the recovered $A(V)$ is ± 0.010 and ± 0.019 for high and low SNR, respectively. In Fig. 10, 11, and 12, we show the best-fit parameters (output) as function of the model parameters (input). We also show the fraction of correctly identified systems using the likelihood ratio test. We only show the results for SMC at high SNR since no absorbers are recovered at low SNR.

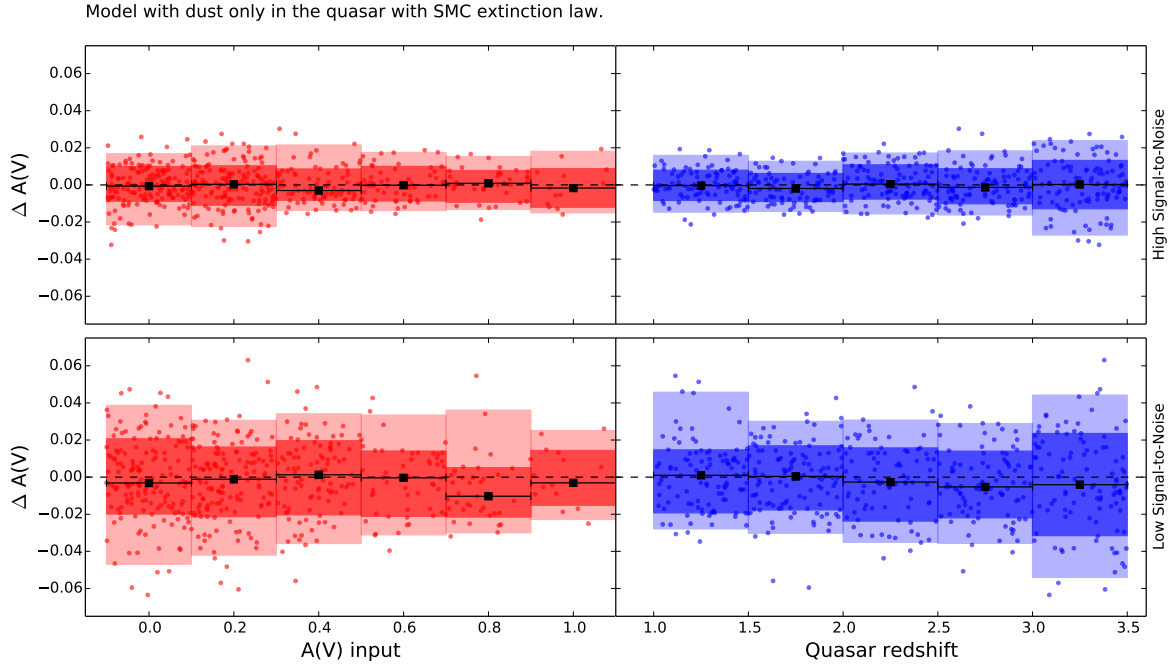


Fig. 9.— Residuals of the recovered $A(V)$ in the null model tests where we only add reddening at the QSO redshift. The top row shows the results of modelling at high SNR, while the bottom row shows the results obtained at low SNR. In each row, the left panel shows the residuals of the best-fit $A(V)$ as function of the input $A(V)$. The right panel shows the same residuals as function of QSO redshift. We observe no bias (i.e., no systematic offset in the residuals) and no significant dependence on input parameters.

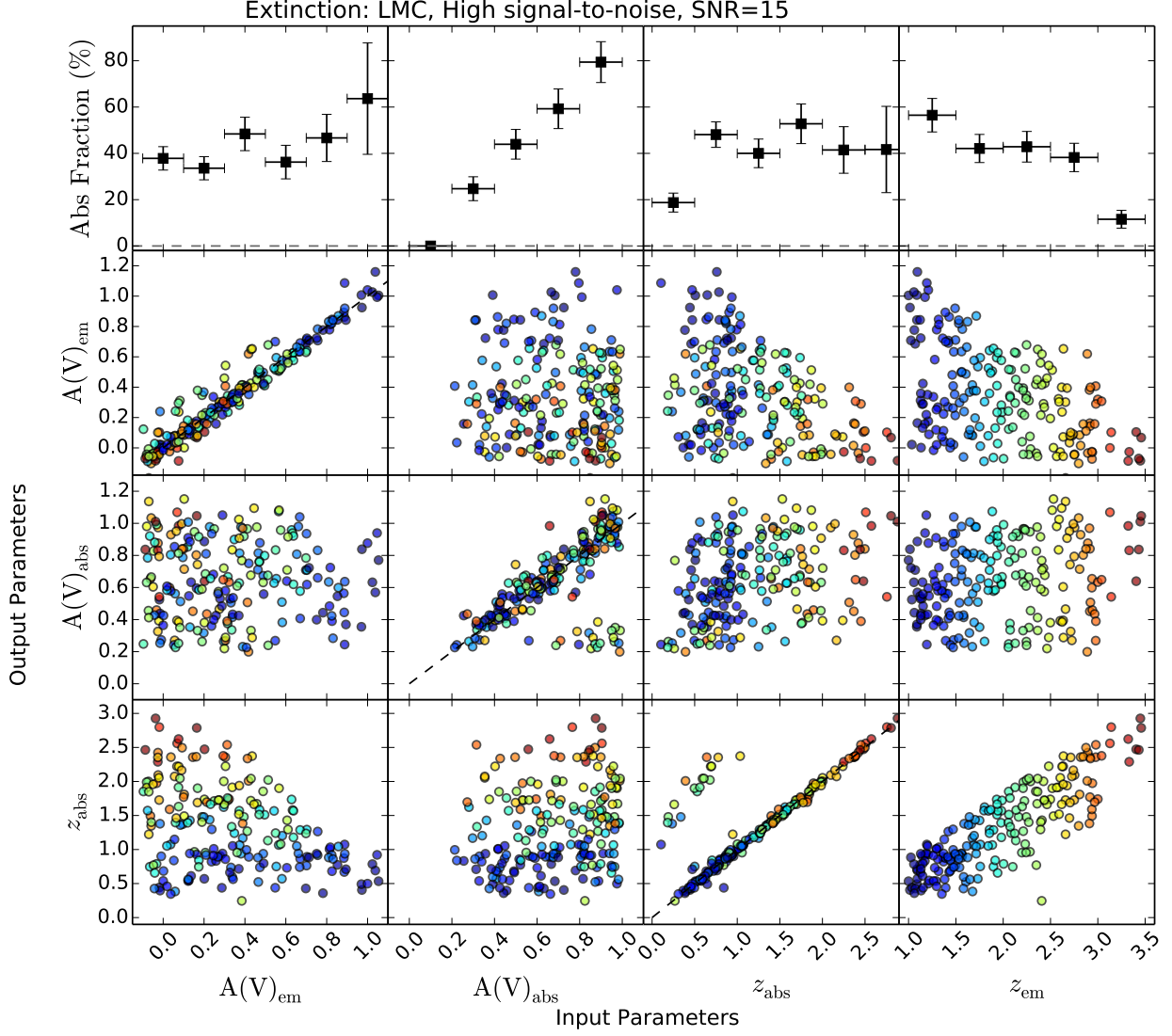


Fig. 10.— The top row shows the recovered fraction of correctly identified absorbers using the likelihood ratio test and in the three subsequent rows, we show the best-fit output parameters as function of the input parameters. The data shown are for model runs with high SNR and assuming the LMC extinction curve. We only show the results for the correctly identified absorbers. The points are colour-coded by redshift of the QSO (blue corresponds to $z = 1$, and red indicates $z = 3.5$).

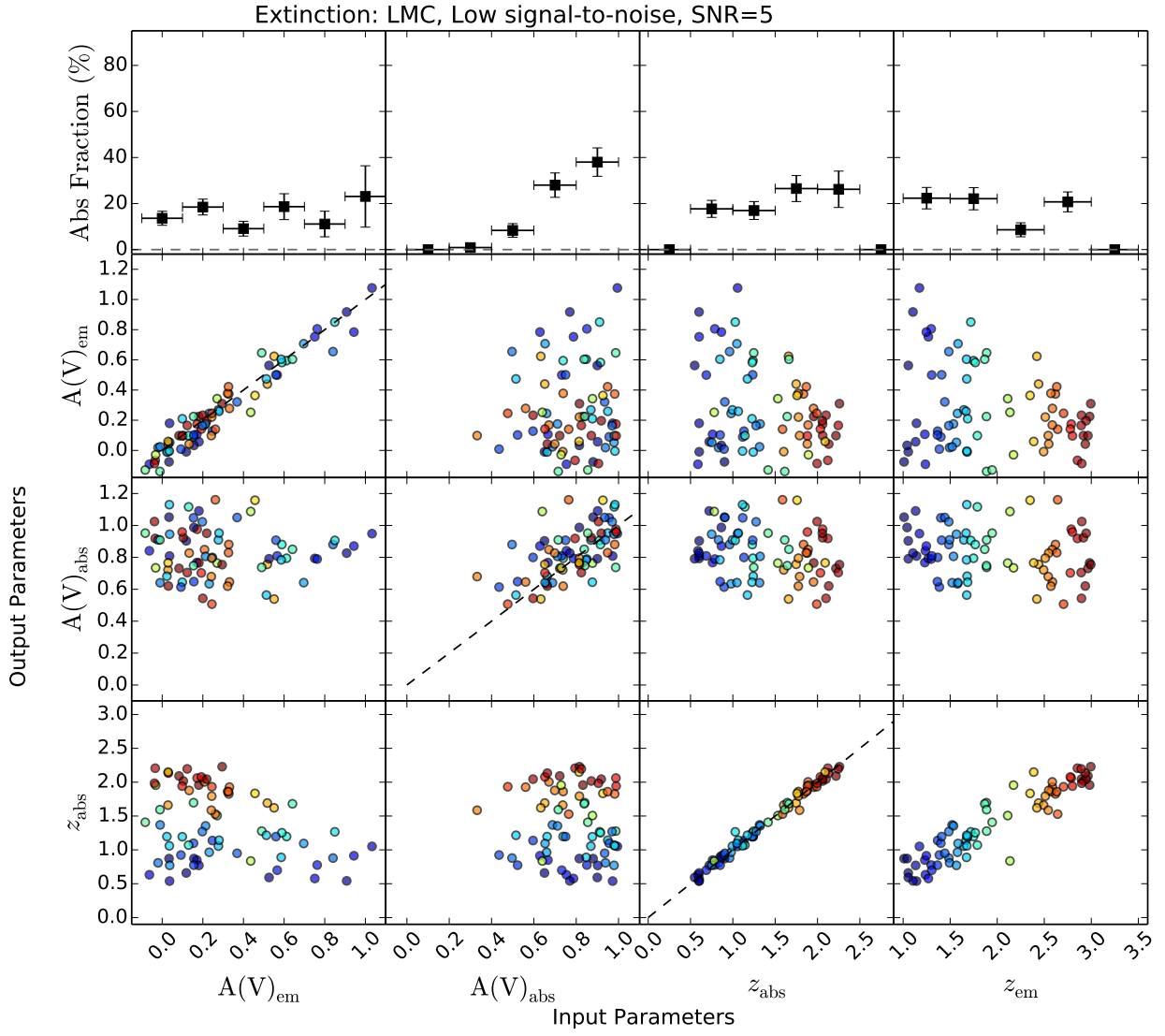


Fig. 11.— Same as Fig. 10 but for low SNR assuming the LMC extinction curve.

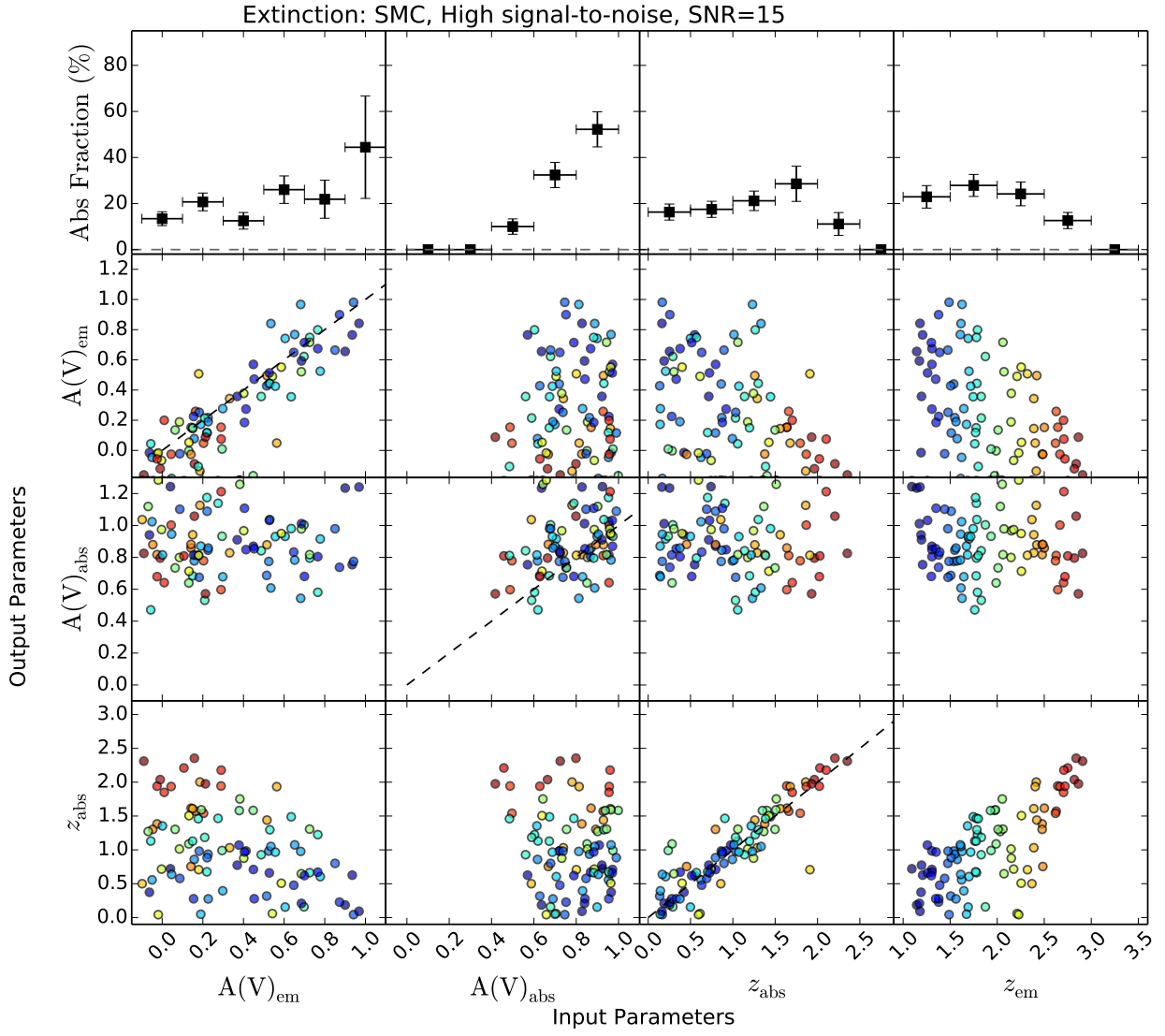


Fig. 12.— Same as Fig. 10 but for high SNR assuming the SMC extinction curve.

C. Individual SEDs

Fig. Set 13. Spectral Energy Distributions

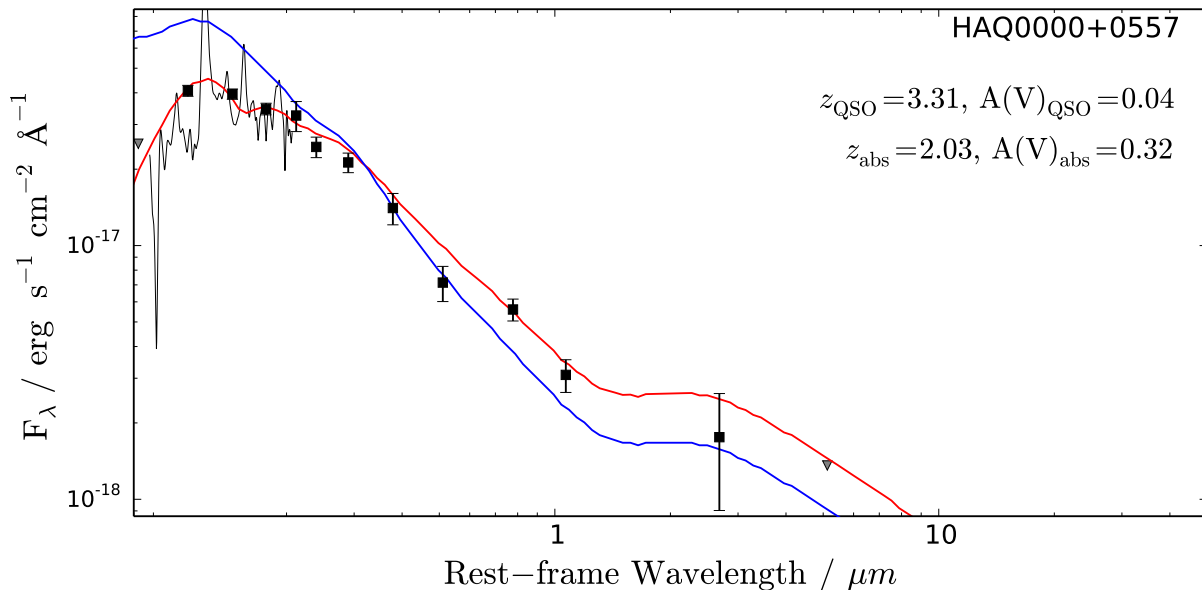


Fig. 13.— Spectral energy distribution from photometry from SDSS, UKIDSS and WISE. The NOT spectra have been smoothed for visual purposes. We show the continuum template from Richards et al. (2006) reddened by the amount of reddening inferred from fitting the spectra (*red line*). In blue we show the unreddened template. Upper limits (2σ) are shown as grey triangles. (The full set of figures is available on the survey webpage <http://www.dark-cosmology.dk/~krogager/redQSOs/data.html>)

D. QSOs with intervening absorbers from statistical modelling

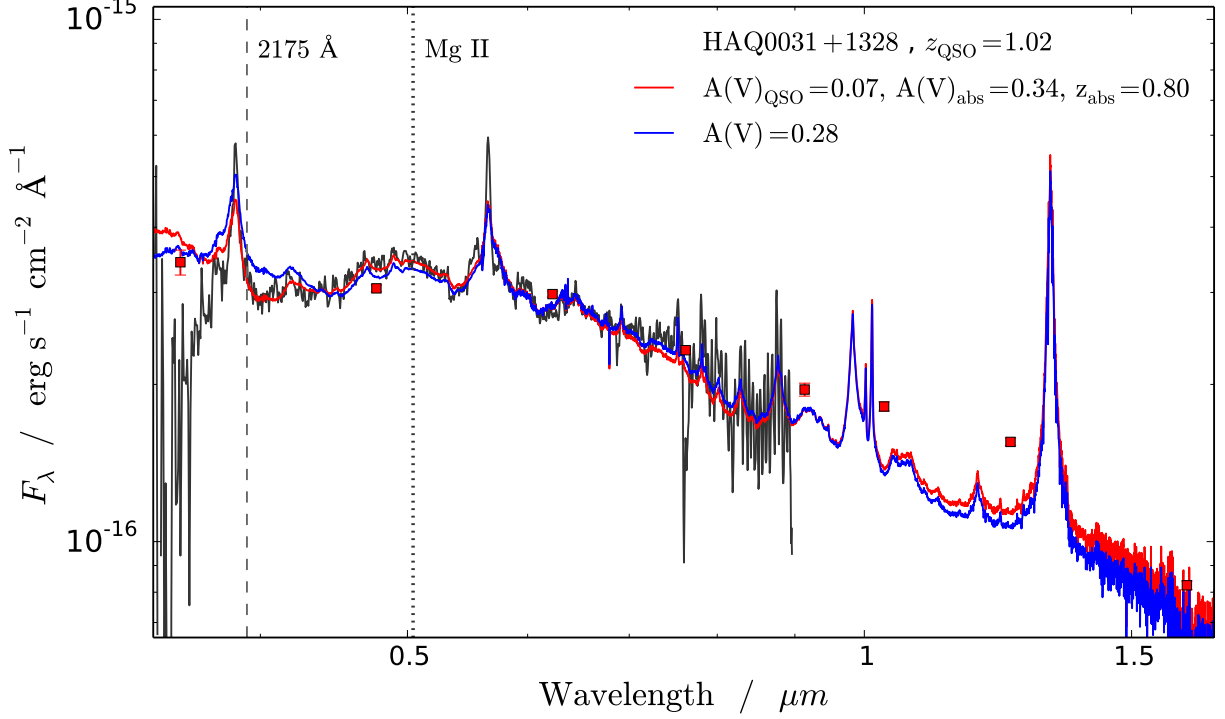


Fig. 14.— Spectra and photometry for the QSOs with preferred dust in an intervening absorption system. The figure shows the spectral data in black and the SDSS and UKIDSS photometry as red squares. In cases where both SDSS and NOT spectra are available, we show the SDSS spectrum as black and the NOT spectrum in gray since the SDSS spectrum was used in the analysis. The SDSS spectrum, if available, has been smoothed with a 3-pixel Gaussian kernel for presentation purposes. The blue and red templates show the best-fit null model and general model, respectively. The dashed and dotted vertical lines indicate the locations of the 2175 Å bump and Mg II at the best-fit redshift for the absorber.

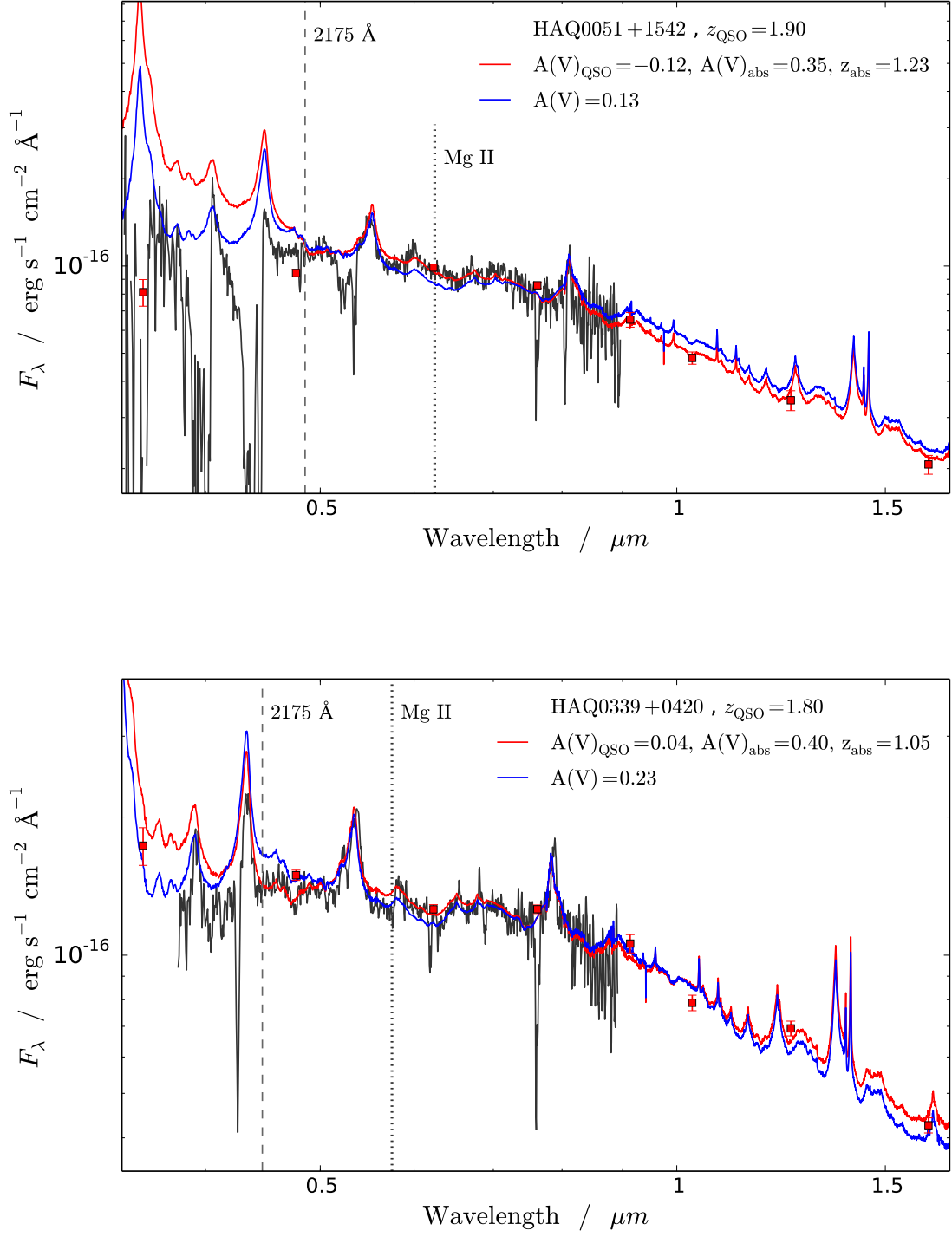


Fig. 14.— Continued.

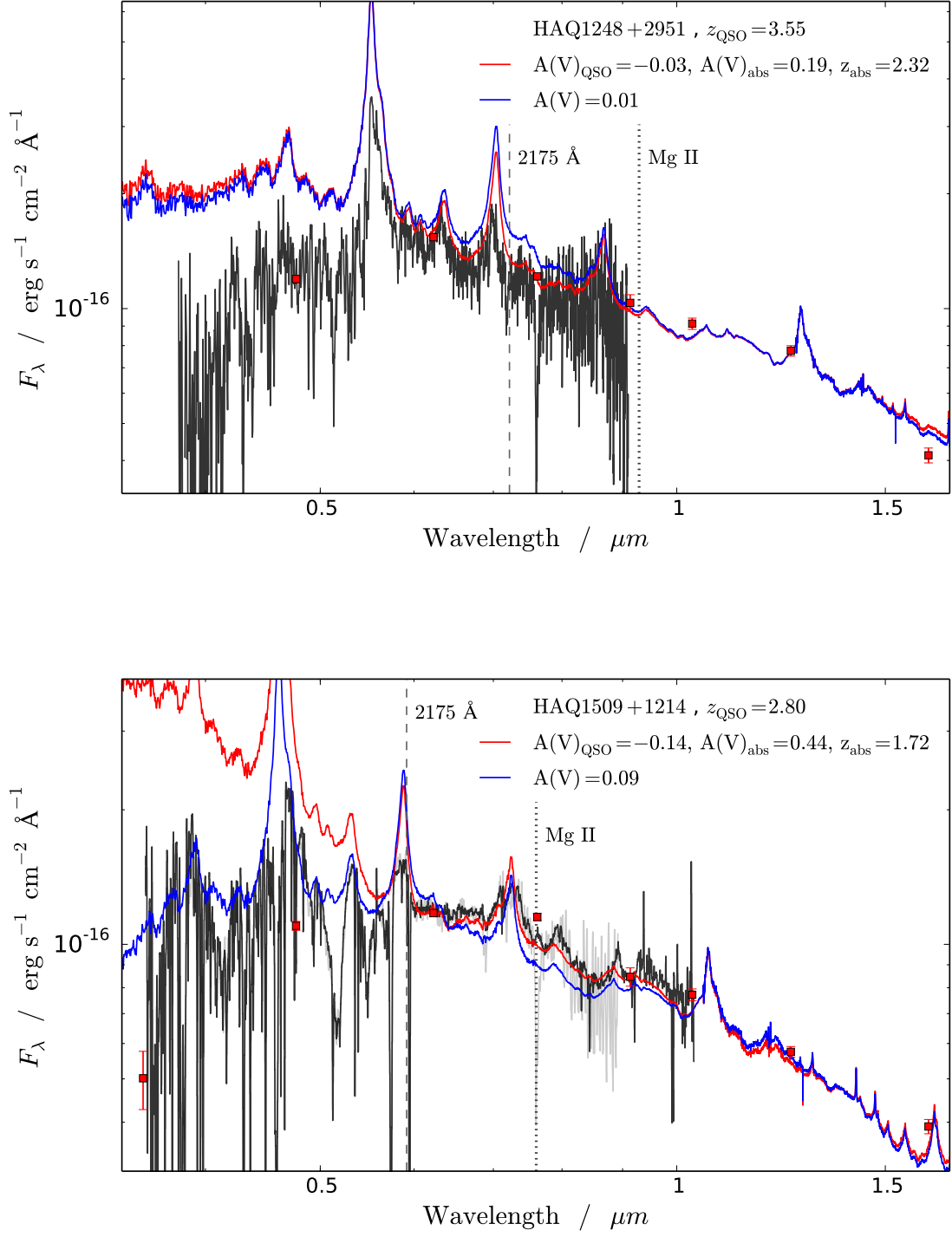


Fig. 14.— Continued.

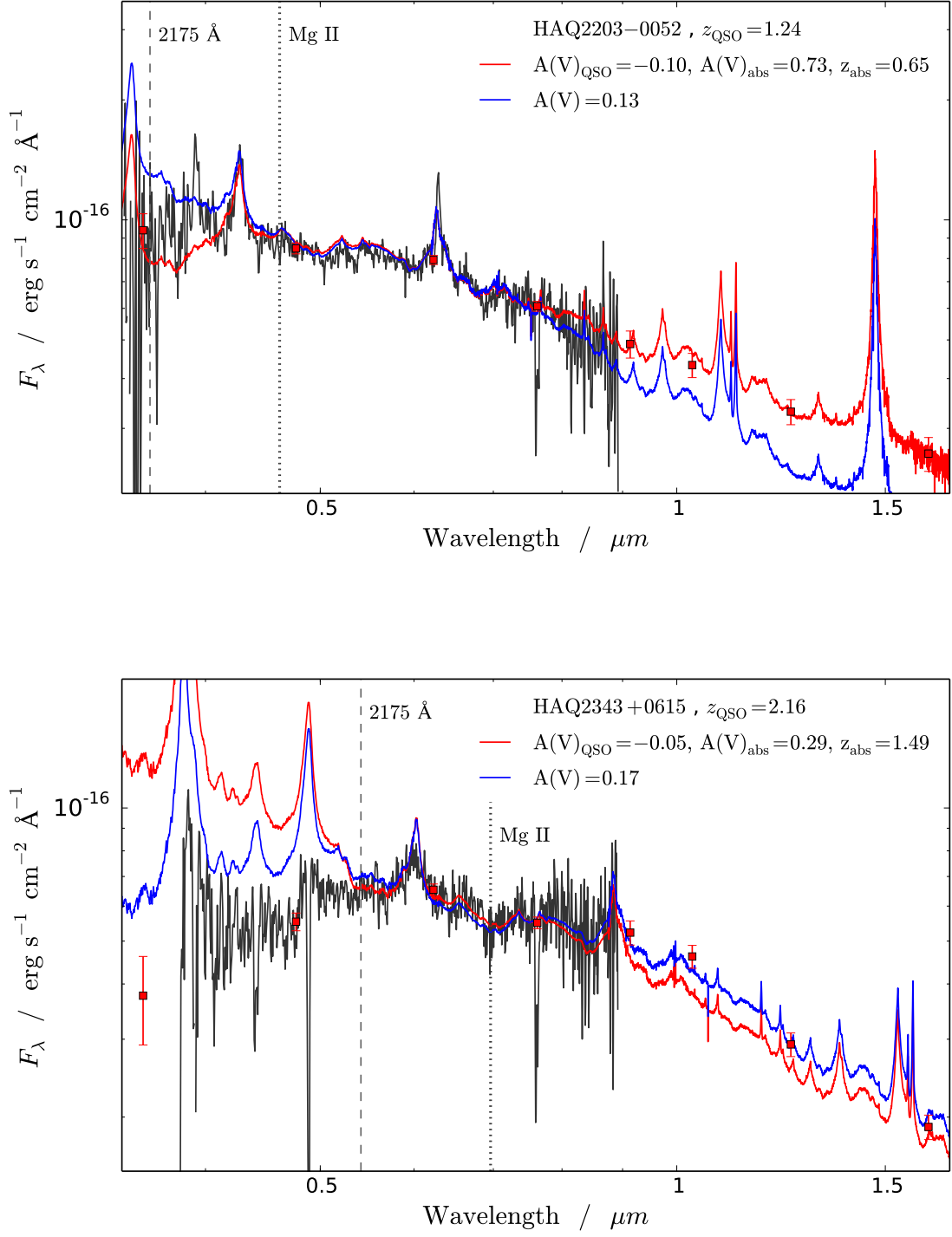


Fig. 14.— Continued.

E. Spectra not classified as QSOs

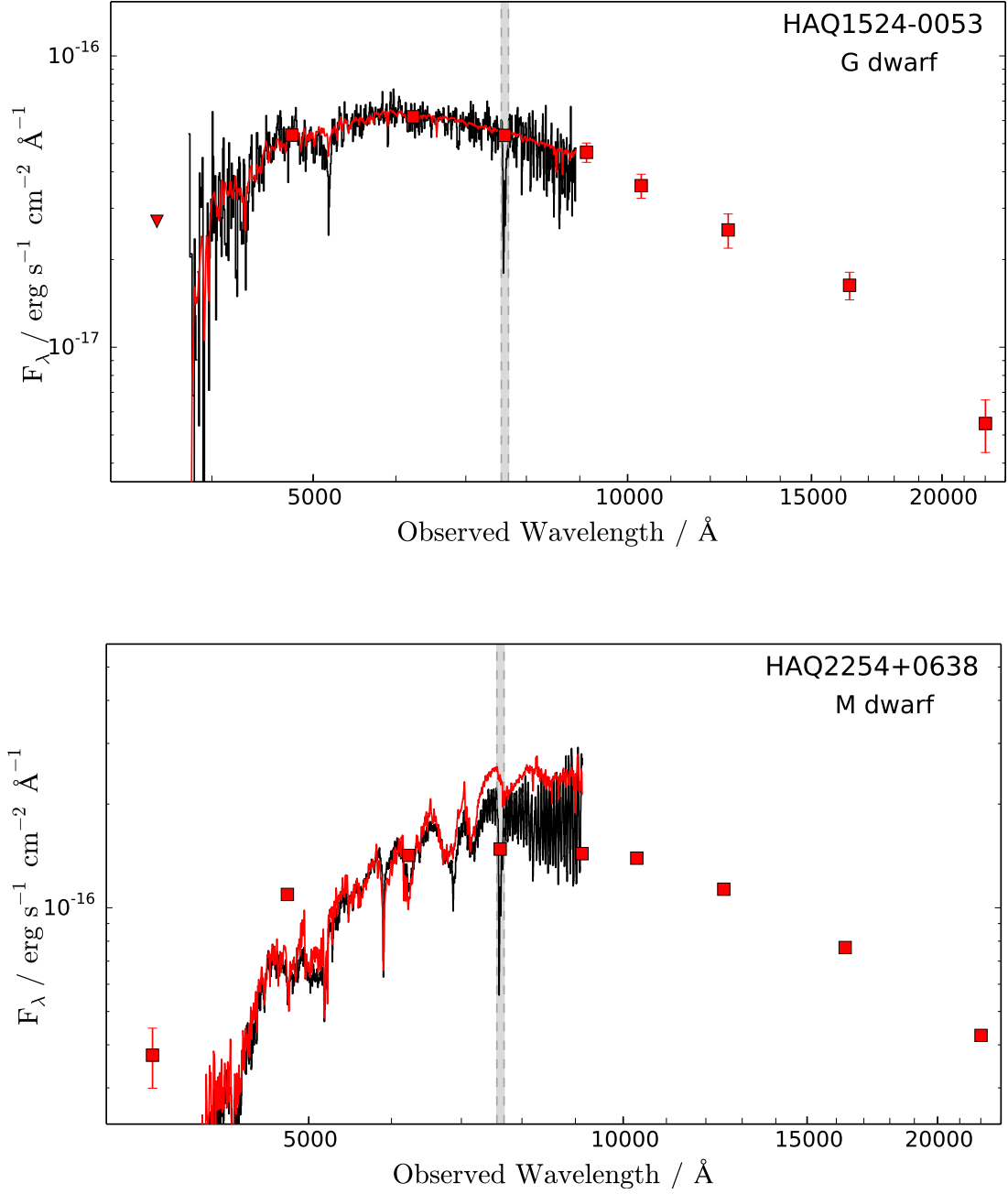


Fig. 15.— The observed spectra are plotted as a solid black line. In each panel, we provide the stellar classification. The red line overplotted is a stellar template to match the observed spectrum. Overplotted with filled squares are the SDSS and UKIDSS photometric data points. The NOT spectra have been scaled to match the r -band photometric data point from SDSS. Note that the spectra have not been corrected for telluric absorption (marked with a grey band at $\sim 7600 \text{ \AA}$).

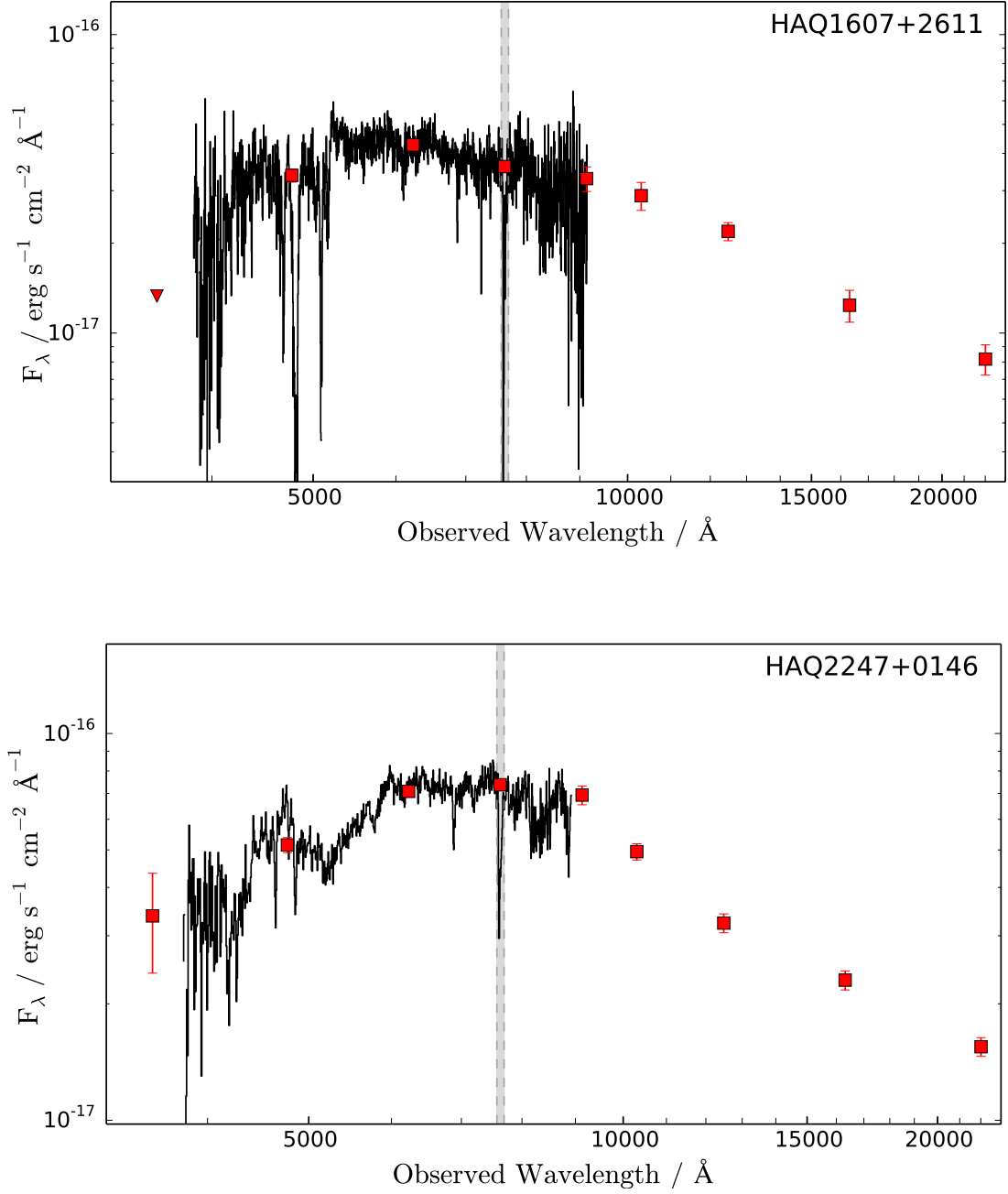


Fig. 16.— Unidentified targets. The observed spectra are plotted as a solid black line. Overplotted with filled squares are the SDSS and UKIDSS photometric data points. In these two cases, we have not been able to securely classify the targets. The NOT spectra have been scaled to match the r -band photometric data point from SDSS. Note that the spectra have not been corrected for telluric absorption (marked with a grey band at $\sim 7600 \text{\AA}$).

F. Candidates

Table 7. Remaining Candidate QSOs.

Target	RA (J 2000)	Dec (J 2000)	r_{SDSS} (AB)
HAQ0000+1250	00 00 08.483	+12 50 33.48	18.84
HAQ0001+0411	00 01 43.455	+04 11 55.69	19.44
HAQ0001+0431	00 01 42.854	+04 31 38.89	19.44
HAQ0003+0221	00 03 43.674	+02 21 29.39	19.17
HAQ0012+1535	00 12 15.986	+15 35 51.08	19.71
HAQ0014+1403	00 14 39.454	+14 03 07.74	19.93
HAQ0015+1213	00 15 10.919	+12 13 53.30	19.85
HAQ0019+0657	00 19 57.289	+06 57 45.71	19.42
HAQ0021+0633	00 21 02.642	+06 33 25.69	19.50
HAQ0022+1049	00 22 44.368	+10 49 02.85	20.09

Note. — Table 7 is published in its entirety in the electronic edition of the journal. A portion is shown here for guidance regarding its form and content.